공학박사 학위논문

Effects of pressure and substrate bias on the film deposition by DC and RF magnetron sputtering considering charged flux

DC와 RF 마그네트론 스퍼터링 시 하전된 플럭스를 고려한 압력과 기판 바이어스가 박막 증착 거동에 미치는 영향

2023년 2월

서울대학교 대학원

재료공학부

안 선 미

Effects of pressure and substrate bias on the film deposition by DC and RF magnetron sputtering considering charged flux

지도 교수 황 농 문

이 논문을 공학박사 학위논문으로 제출함
2023년 2월

서울대학교 대학원
재료공학부
안 선 미

안선미의 공학박사 학위논문을 인준함
2023년 1월

위 원 장 김 미 영 (인)

부위원장 황 농 문 (인)

위 원 장 호 원 (인)

위 원 김 근 수 (인)

위 원 김 다 슬 (인)

Abstract

Effects of pressure and substrate bias on the film deposition by DC and RF magnetron sputtering considering charged flux

Seon Mi Ahn

Department of Materials Science and Engineering

The Graduate School

Seoul National University

In recent years, the generation of charged flux during direct current (DC) and radio frequency (RF) magnetron sputtering and its effects on film deposition were studied. Thus, the deposition parameter that affects the generation of charged flux was examined in both DC and RF sputtering system. In particular, the charging behavior under the argon (Ar) pressure which is utilizing to generate

plasma and the substrate bias were studied.

First of all, effects of sputtering power, working pressure, and bias on the growth rate, crystallinity, and resistivity of Ag thin films deposited by DC magnetron sputtering were investigated. Thin films were deposited on the substrate under the electric biases of − 300, 0, and + 300 V for 30 minutes with sputtering powers of 20, 50, 100, and 200 W and working pressures of 2.5, 5, 10, and 20 mTorr. Under all sputtering powers, the growth rate of the thin film was increased by the positive bias, whereas it was decreased by the negative bias. For example, the film thicknesses were 345.7, 377.9, and 416.0 nm at − 300, 0, and + 300 V, respectively, at a sputtering power of 100 W and a working pressure of 2.5 mTorr. The bias effect was enhanced as the working pressure decreased. Considering the change of the film growth rate according to the bias, the amount of negatively charged flux was estimated to be roughly 10 %. As the working pressure decreased, the crystallinity of the deposited films increased by the positive bias whereas it decreased by the negative bias, which is indicated by the full width at half maximum (FWHM) determined by X−ray diffraction of the Ag (111) peak. The film resistivity had the same tendency. This change in the deposition behavior of the Ag film can be understood as the effect of the charged flux.

In addition, effects of Ar pressure and substrate bias on tungsten

(W) films deposited by RF magnetron sputtering were investigated. W is generally used as a material to replace copper interconnects for semiconductors. It is commonly observed that tungsten thin films deposited by sputtering at room temperature have a metastable β-phase with relatively high resistivity and transform into a stable α-phase with relatively low resistivity under certain conditions. In this study, to obtain W films with low resistivity suitable for interconnect materials for semiconductors, we tried to identify deposition parameters for the formation of α-phase W by varying the substrate bias and argon (Ar) pressure in an RF magnetron sputtering system. In the initial stage for 1 s of deposition under 20 mTorr and a substrate bias of -100 V, β-phase W nanoparticles were observed using transmission electron microscopy (TEM). However, as the deposition time increased to 10 min under the same pressure and bias condition, the W film became a mixture of α- and β-phases. The fraction of α-phase W increased further as the negative bias increased from -100 to -200 V. In addition, the film density increased and the surface roughness decreased as the bias changed from +100 to -100 V. These results indicate that the negative bias triggered the phase transformation of W from β to α. The bias effect on the formation of α-phase W and film resistivity became more pronounced as pressure increased.

Furthermore, inductively coupled plasma (ICP) was installed in the DC magnetron sputtering system to increase the ionization rate during DC sputtering. W thin films were deposited at substrate biases of −200, 0, and +200 V with increasing the ICP power from 0 to 200 W. The growth of α−phase W was enhanced and the resistivity of W film decreased when the ICP power was increased and a negative bias was applied to the substrate. However, from the X−ray diffraction (XRD) data and resistivity measurement results, it is shown that there are optimized process conditions for growing α−phase W. The W thin film with the lowest resistivity in this study was obtained when the ICP power was 100 W and the substrate bias was −200 V.

Keyword : Charged flux · Sputtering · Thin film · Tungsten · Silver

Student Number : 2018−27919

List of Figures

List of Tables

Table of Contents

Chapter 1. Introduction

1.1. Non-classical crystallization

In classical crystallization, the way individual atoms grow into crystals is determined by the surface state. When atoms sit on the atomically rough interface with lots of kink sites, they usually result in diffusion-controlled growth as there is no barrier to atomic incorporation. On the other hand, when atoms land on the terrace on the smooth interface, they diffuse into the ledge and finally coalesce in the kink into crystals. This concept is called 'terrace ledge kink (TLK)' model [2]. Atoms which adsorb on a terrace generate excess energy, whereas atoms at the kink site do not provide excess energy. Therefore, atoms are incorporated only at the kink site and grow as a whole.

However, numerous evidences indicating that crystals grow by the building block of nanoparticles (NPs), which is called non-classical crystallization, have been reported [3-9]. In addition, recent observations by in-situ transmission electron microscope (TEM) support that the building block of crystal growth is NPs [10,

11].

1.1.1. Theory of charged nanoparticles

A ‘theory of charged nanoparticles (TCN)’, which is non-classical crystallization mechanism, that charged nuclei were formed in the gas phase during synthesis of diamonds in chemical vapor deposition (CVD) process was first proposed as a charged cluster model by Hwang et al. [1]. After that, the TCN emphasizing the importance of charge on the crystal growth was introduced [12], and it has been extensively studied especially in CVD process.

During hot wire CVD process, diamond was deposited on a silicon substrate while soot was deposited on an iron substrate under the same deposition conditions as shown in Fig 1.1. This result indicated that the charge transfer rate of the substrate affected the deposition behavior. In other words, charged nanoparticles (CNPs) formed in the gas phase lose their charge on the Fe substrate with high charge transfer rate, whereas they retain their charge on the Si substrate with low charge transfer rate. The different deposition behavior of CNPs and neutral nanoparticles (NNPs) implies that the charge enhanced diffusion or chemical kinetics. NNPs are coagulated by random Brownian motion and become porous structures. On the other

hand, CNPs undergo self-assembly and oriented attachment to form crystalline structures.

1.1.2. Charge enhanced kinetics

To explain the charge-enhanced kinetics, it must be assumed that the charge weakens the bond strength. If the charge weakens the bond strength, CNPs will have liquid-like property. Clare et al. [13] published ab initio calculations studying the effect of charge on the bond strength in hydrogenated amorphous silicon. In the presence of a single negative or positive charge, the charge effect on the strength of a silicon-silicon (Si-Si) and silicon-hydrogen (Si-H) bonds in the molecules SiH_4 and Si_2H_6 was calculated. The results of ab initio calculations are summarized in Table 1.1. When atoms are embedded in the lattice, they will not be free to be arranged into molecular geometries that resemble optimized ion geometries. Instead, they will be able to relax to some extent. Therefore, the actual charge effects on the bond strength will be between the unoptimized (adiabatic) and optimized results, close to the unoptimized value. It has been shown that both positive and negative charge weaken Si-Si and Si-H bonds.

The effect of charge on the bond strength can also be explained by bond order. A bond order, which is the number of chemical bonds between a pair of atoms, indicates the strength or stability of a bond. The bond order is defined as half the difference between the number of electrons in bonding and antibonding orbitals as expressed by the following equation,

$$\text{Bond order} = \frac{No.of\ bonding\ electrons - No.of\ antibonding\ electrons}{2} \qquad (1.1)$$

When electrons are added to antibonding orbitals (negatively charged) or electrons are removed from bonding orbitals (positively charged), the bond order decreases in both cases. Therefore, both positive and negative charge weaken the bond strength.

Recently, many experimental results are published supporting that charge enhances atomic diffusion or chemical kinetics. Fujita [14] has studied the magic size where the material behavior is changed abruptly and observed the coalescence between clusters of atoms in a coherent orientation when they came into contact with each other. On the other hand, Ijima and Ichihashi [15] observed that a continuous change in the shape of small gold particles through an internal transformation by TEM with a real-time video recording system. It has been known that the dynamic behavior of metal nanoparticles in TEM is due to the thermal energy of momentum transfer by incident high-energy electrons. However, the

accumulation of electron charge on the TEM specimen, which was unavoidable, was neglected when interpreting the experimental results.

Kim et al. [16] investigated the putative mechanisms and the importance of charge using carefully designed experiments. Highly-conductive few-layer graphene and insulating silicon monoxide (SiO) membranes were compared to examine the behavior of Au NPs. The coarsening of Au NPs by coalescence was noticeable on SiO but was negligible on the grounded graphene. In addition, the coalescence of two Au NPs, which occurred during TEM observation, was faster on the insulating few-layer hexagonal boron nitride (h-BN) than on the grounded graphene membrane. These results showed that the rapid coalescence and active fluctuation of Au NPs during TEM observation are mainly caused by the charge build-up in NPs and not by electron bombardment.

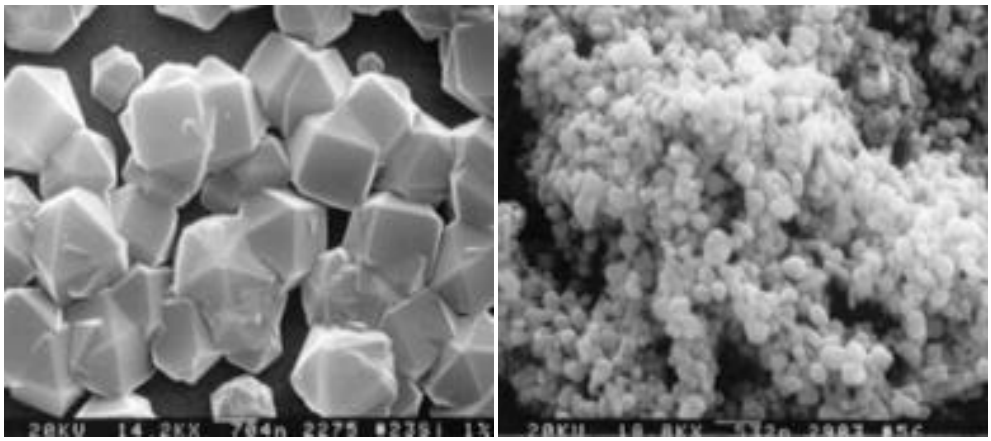

Figure 1.1 SEM microstructures of (a) diamond deposited on the silicon substrate and (b) soot deposited on the iron substrate [1]

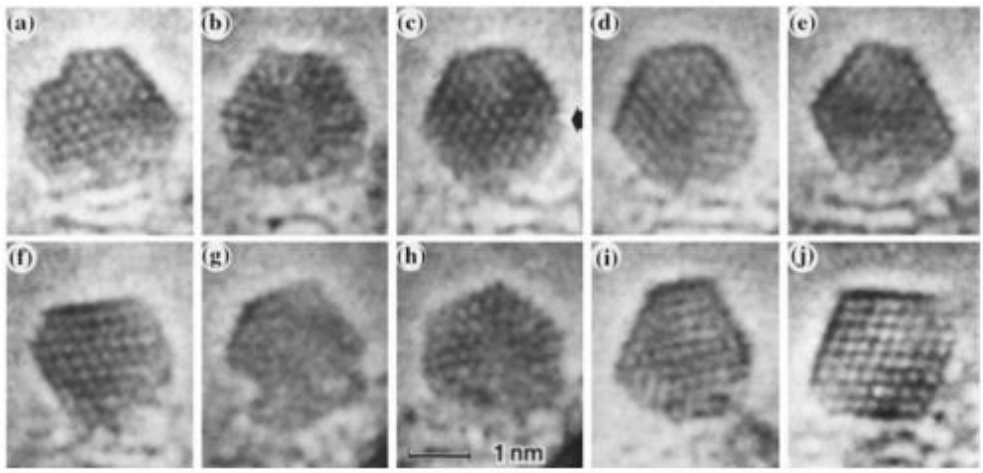

Figure 1.2 TEM observation of various shapes of an ultrafine particle consisting of about 460 gold atoms reproduced from a video tape recorder. The shape of the particle itself was changing continually under electron-beam irradiation. The particles in (a), (d), and (i) are single twins. Single crystals with cuboctahedral shape are seen in (e), (f), and (i). From the size of the cuboctahedron (j), the particle theoretically contains 459 gold atoms. The particle also transforms into a multiply twinned icosahedral particle, (b) and (h) [15]

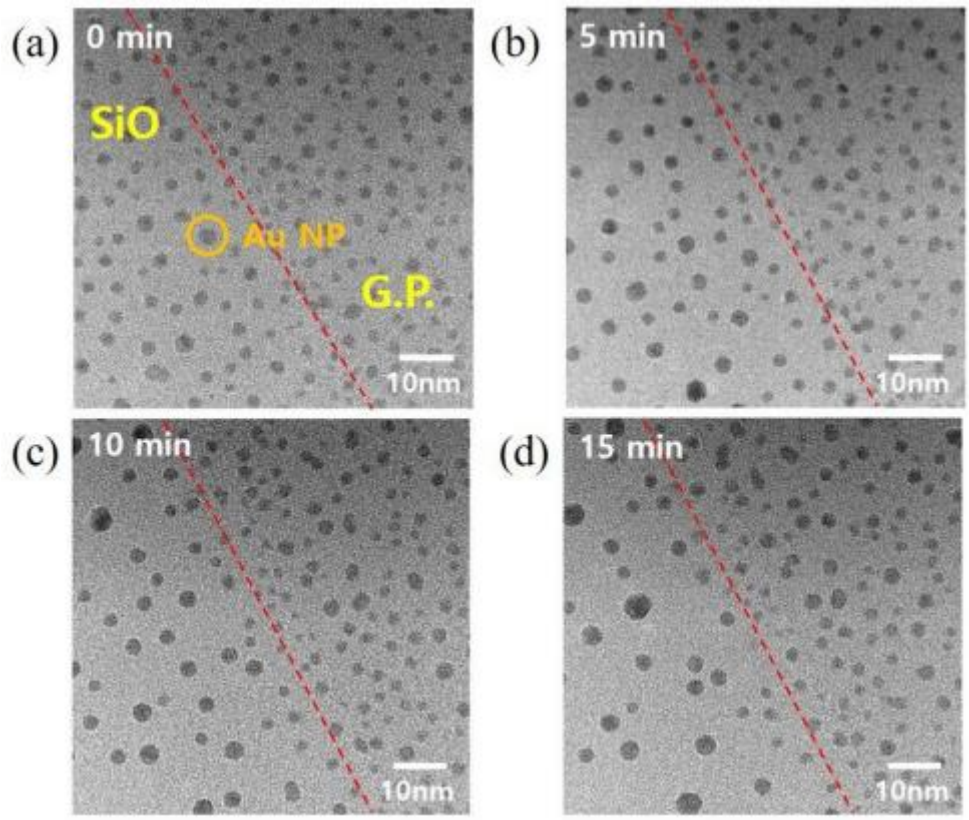

Figure 1.3 The time evolution TEM images of Au NPs on the grounded graphene and the SiO membrane at (a) 0, (b) 5, (c) 10, and (d) 15 min [16]

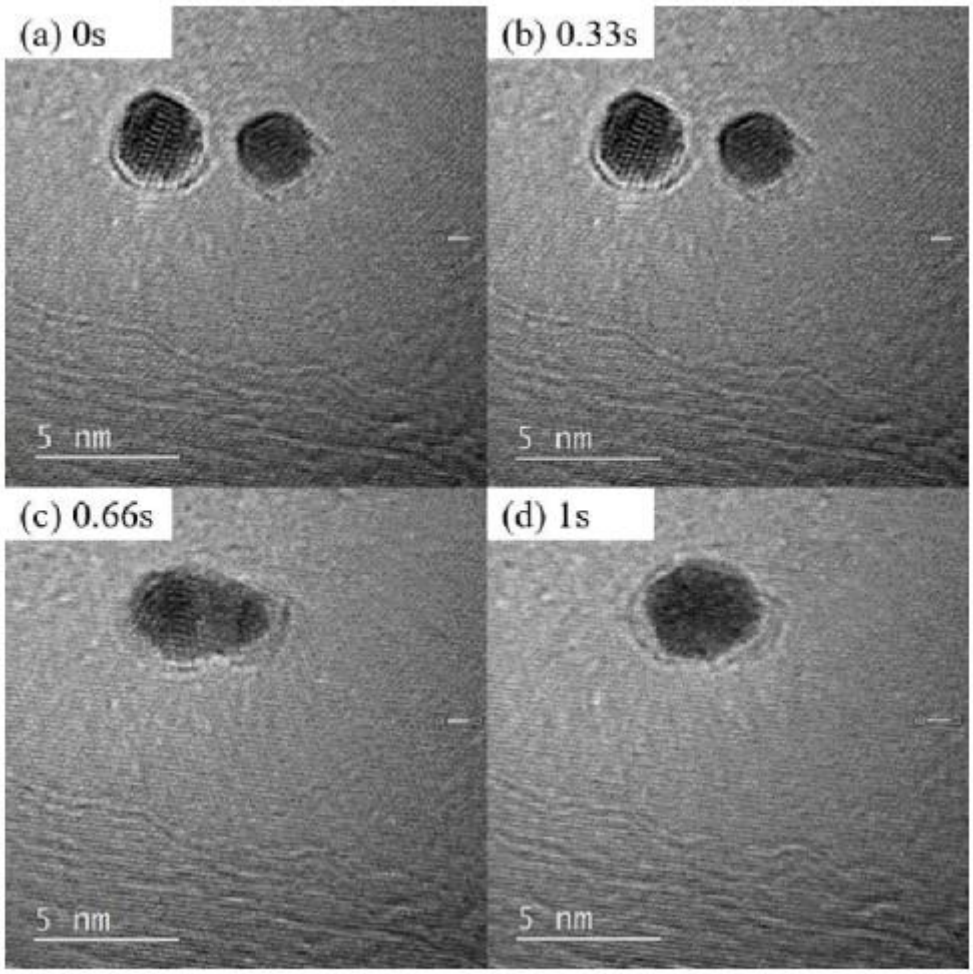

Figure 1.4 The time evolution of coalescence of two Au NPs on the insulating h-BN substrate. The coalescence is completed after 0.66 s. The orientation of two Au NPs in (a)-(c) was different [16]

Compound	Si−H (eV)	Si−Si (eV)
SiH_4 (optimized)	3.9	−
SiH_4^- (optimized)	0.98	−
SiH_4^+ (optimized)	0.30	−
Si_2H_6 (optimized)	3.5	3.2
$Si_2H_6^-$ (optimized)	1.02	1.11
$Si_2H_6^+$ (optimized)	1.59	1.6
SiH_4^- (unoptimized)	1.35	−
SiH_4^+ (unoptimized)	0.09	−
$Si_2H_6^-$ (unoptimized)	1.34	1.3
$Si_2H_6^+$ (unoptimized)	1.49	1.6

Table 1.1 Summary of Si−H and Si−Si bond strengths [13]

1.2. Physical vapor deposition (PVD)

PVD is a vacuum deposition method that can be used to deposit or coat thin films including metals, ceramics, glass, and polymers. The difference of PVD from chemical vapor deposition (CVD) is that the primary source of the depositing species is a solid or liquid, rather than a gas, and has a vapor pressure that is much lower than the working pressure of the deposition system [17]. PVD has a process of converting a source material, which exists as a condensed phase, into a vapor phase, and then converting it back into a thin film-shaped condensed phase. The two most common PVD methods are evaporation and sputtering. PVD is used in the manufacturing applications that require thin films such as semiconductor devices [18], microelectronics [19, 20], and metalcutting applications [21].

1.2.1. Sputter deposition

Sputter deposition is one of the PVD processes that deposits thin films by sputtering. The sputtering process is as follows. An inert gas such as argon (Ar) is ionized by collisions with electrons. The reaction for the formation of ions (Ar^+) can be described by:

$$e^- + Ar \rightarrow Ar^+ + 2e^- \quad (1.2)$$

Ar cations are then accelerated by the electric field between a target material (cathode) and a substrate (anode). When Ar ions, which have high enough energy to brake bonds between atoms of the target material, collide with the target surface, atoms or particles are ejected. The sputtered particles cross the vacuum chamber and they are condensed as immediately as they land on the substrate. An industrial application of sputtering is the sputter deposition.

The sputtered particles typically have a broad energy distribution of up to several tens of eV. At lower gas pressures, they can fly ballistically in a straight line from the target material and energetically crash into the substrate. As a result, the deposited material on the substrate is re-emitted by a bombardment, which is called resputtering [22, 23]. At higher gas pressures, the sputtered particles collide with gas atoms acting as moderators, resulting in a random walk. This is related to mean free path. The mean free path is the average distance that a moving particle travels before it undergoes a substantial change in direction or energy, typically as a result of one or more successive collisions with other particles. The mean free path λ can be approximated by [24, 25]

$$\lambda = \frac{k_B T}{\sqrt{2}\pi d^2 p} \quad (1.3)$$

where k_B is Boltzmann's constant, T is temperature, d is a radius of the gas, and p is the pressure. By changing the gas pressure, the mean free path and the collision frequency are changed. Therefore, this allows for full range varying from high-energy ballistic impacts to low-energy thermalized motion.

Reactive gases can be used to deposit compounds during sputtering, which is called reactive sputtering. The sputtered particles undergo a chemical reaction either in flight or on the substrate, depending on the process parameters. For example, reactive gases introduced into the sputtering chamber, such as oxygen or nitrogen, can create oxide and nitride films, respectively [26].

Although the many parameters available to control sputter deposition give complexity to the process, the strength lies in the ability to control the growth and microstructure of the film. A significant advantage of sputter deposition is that materials with very high melting points are easily sputtered, whereas evaporation of these materials in a resistive evaporator is difficult or impossible. Furthermore, films deposited by sputtering generally have better adhesion to the substrate than films deposited by evaporation. The

advantage of sputtering over evaporation is also that sputtering can be done top-down while evaporation has to be done bottom-up. Compatibility with reactive gases such as oxygen is another advantage, as the sputtering sources do not contain hot parts and are usually water cooled to avoid heating.

One of disadvantage of the sputter deposition is that the patterning of the target material on the surface of the substrate is difficult. This is because sputtering has the diffuse-transport characteristic, which makes a full shadow impossible. Therefore, it is not possible to completely restrict where atoms go, which can lead to contamination problems. In addition, compared to pulsed laser deposition, active control for layer-by-layer growth is difficult, and an inert gas can be embedded in the growing film as an impurity.

1.2.2. Direct current (DC) sputtering

Conventional DC sputtering system comprises of a pair of planar electrodes, one of which is a target as a cathode, and the substrate, mounted on the anode, is grounded [27]. The outer of the cathode is cooled by water. To initiate a glow discharge, the gas pressure in the chamber is kept constant and a voltage of several kilovolts (kV) is applied between the electrodes. The gas pressure can be maintained

by flowing Ar gas at a certain rate. The positive Ar ions in the plasma are then accelerated toward the cathode and sputter the target surface. If the cathode of a DC diode system, which is the target, is an insulator, a charge build-up can be formed on the surface of the target that prevents ion bombardment. Therefore, the target must be conductive. In the conventional DC sputtering system, which is the DC diode sputtering system, the deposition rate is low and there is intense electron bombardment of the substrate which can cause thermal and structural damages. These problems can be solved by generating a magnetic field using an appropriate arrangement of magnets. A system in which magnets are mounted on the cathode is called a DC magnetron sputtering system.

In DC magnetron sputtering systems, a magnetic field can be used to increase the electron density by keeping the electrons closer to the target surface. A high electron flux generates a high-density plasma, by increasing the probability of ionizing a neutral molecule of the gas. A higher ion concentration results in more sputtering and, consequently, an increased deposition rate. This enables sputtering at low pressure.

1.2.3. Radio frequency (RF) sputtering

In DC sputtering systems, there is a limitation that the target should be metal. If an insulator target is used, a positive charge will be immediately accumulated on the insulator surface, preventing the glow discharge from sustaining. By using a RF power supply instead of a DC power supply, it is possible to maintain a glow discharge while using an insulator as a target. This system is called a RF sputtering system.

In RF sputtering systems, an impedance matching network is used to couple the maximum amount of power to the plasma by reducing reflected power and should be placed close to the RF electrode [28]. When an RF sputtering system is operated at 13.56 MHZ with a peak-to-peak voltages of greater than 1000 volts (V) [29], a positive-negative voltage appears alternately on the surface of the electrode. During half of a cycle, the negative potential accelerates the positive ions toward the surface with enough energy to sputter. During the other half of a cycle, the positive potential attracts the electrons, which neutralize the positive ions and prevent the accumulation of positive charge.

Compared to DC sputtering systems, RF sputtering systems have several advantages including the use of insulator as targets. An RF sputtering system is one of methods of avoiding arcs. Arcing can be prevented by periodically discharging the accumulated charge on the

surface of the cathode [26]. In other words, plasma arcing and layer quality control issues are eliminated, resulting in more uniform layer deposition. In addition, 'race track erosion' on the surface of the target is reduced in RF sputtering systems. It has been known that erosion occurs in a racetrack zone, where the magnetic field lines are parallel to the target surface during magnetron sputtering [30]. Since the large ionization volume greatly increases the area of erosion [31], an RF sputtering system can decrease the race track erosion on the target surface, and therefore, the lifetime of the target increases.

1.3. Purpose of this study

Theory of charged NPs and charge enhanced kinetics have been confirmed by many experiments and calculations. The generation of CNPs was confirmed during CVD process and their liquid-like behavior was observed by TEM. Many books and papers have been published on this theory.

Although this theory was applied well to the CVD process, its application in the PVD process still required further investigation. Recently, several studies using RF and DC magnetron sputtering systems have confirmed the generation of charged NPs. Ti NPs were investigated during RF sputtering and Ag NPs were studied during DC sputtering. Since the experimental results according to the PVD equipment and materials are still insignificant, more research on this is needed.

Therefore, the main purpose of this Ph. D course is to verify the effect of charged flux generated during RF and DC sputtering on thin film deposition. To adjust the amount of the charged flux generated and investigate its effect, experiments were conducted with two key deposition parameters considered: operating pressure and substrate bias.

Chapter 2. Effects of Sputtering Power, Working Pressure, and Electric Bias on the Deposition Behavior of Ag Films during DC Magnetron Sputtering Considering the Generation of Charged Flux

2.1. Introduction

Ag thin films and nanoparticles are known to have excellent electrical and optical properties, excellent chemical and thermal stability, and bactericidal effects, and therefore, they are used in various fields such as optical applications [33-37], microelectronics

[38, 39], and biomedical applications [40-42].

The mechanism of crystal growth has been explained by a so-called terrace-ledge-kink (TLK) model [2], in which an atom, ion, or molecule is adsorbed on the terrace, migrates to the ledge, and incorporates into a crystal at the kink. This growth mechanism can be called classical crystallization in comparison with non-classical crystallization, which has been studied extensively in these years. Many puzzling growth features that are difficult to explain with the existing TLK model have been reported. To explain such puzzling features, non-classical crystallization, where the building blocks of crystal growth are nanoparticles [43-55], was suggested. Non-classical crystallization has been studied intensively in solution, where the growth details are revealed by the in-situ transmission electron microscope (TEM) using a liquid-cell technique [10, 56-58].

Hwang [59] has done a lot of researches on non-classical crystallization in thin film growth by chemical vapor deposition (CVD). They suggest 'the theory of charged nanoparticles (TCN)' as a new crystal growth mechanism. According to the TCN, electrically charged nanoparticles are first generated in the gas phase, and thin films are grown by the building block of these charged nanoparticles during the CVD process. In this case, the crystal growth unit is

nanoparticles, not atoms nor molecules, where charge plays a very important role in the evolution of dense crystalline films. The charge is suggested to enhance kinetics and to make nanoparticles liquid-like. As a result, charged nanoparticles tend to produce dense films with high crystallinity whereas neutral nanoparticles tend to produce porous films with low crystallinity. For example, in the presence of charged silicon nanoparticles, the deposition behavior was compared between the floating and grounded silicon substrates during CVD [60]. The nanowires of single crystalline silicon or dense films grew extensively on the floating substrate whereas nanoparticles or porous films were deposited on the grounded substrate. As another example, Park et al. [61] deposited a fully epitaxial silicon film on a silicon wafer at 550 ° C under the substrate bias of-1000 V during radio frequency plasma-enhanced chemical vapor deposition (RF-PECVD). It is due to the liquid-like nature of charged nanoparticles. Lee et al. [62] used bipolar charging by corona discharge and thereby could decompose SiH4 at low temperature, which made it possible to deposit the silicon film at 500oC at a rate 5.6 times higher than that of the conventional thermal CVD. Besides, Kim et al. [63] could grow SiC epitaxial films using the charged nanoparticles generated during hot wire CVD.

Recently, the possibility of non-classical crystallization for the

film growth in physical vapor deposition (PVD) is actively underway. Jeon et al. [64] confirmed the presence of charged Ag nanoparticles through a bias experiment in the evaporator. Jang et al. [65] studied the existence of charged Ag nanoparticles in DC magnetron sputtering and their contribution to Ag films deposition behavior. Also, Kwon et al. [66, 67] studied the existence of charged Ti nanoparticles in the RF magnetron sputtering reactor and their effect on Ti film deposition. However, a lot of researches are still needed to understand the deposition behavior in PVD, which had not been understood by the classical mechanism.

In this study, the possibility for the generation of charged flux is studied during DC magnetron sputtering of Ag. Ag films were deposited while varying the sputtering power and working pressure under the condition where the electric bias is applied to the substrate. The film thickness was measured by observing the cross-section of deposition films by field-emission scanning electron microscopy (FESEM). The film crystallinity and resistivity were analyzed, respectively, by X-ray diffraction (XRD) and a four-point probe.

2.2. Experimental

Fig. 2.1a shows a schematic of the DC magnetron sputtering

reactor. The Ag target of 99.999% purity and 7.62 cm diameter was used. The plasma was generated by a DC power supply (PSPlasma, Inc., SDC1022A, Hwaseong, South Korea) connected to the Ag target. The distance between the substrate holder and the Ag target was 12 cm. As shown in Fig. 2.1b, the substrate holder was placed on the insulating glass to make it electrically floating from the grounded chamber in order to apply the electric bias. To minimize the effect of the substrate holder bias on the plasma, the Cu grounded mesh was placed above the substrate holder. The hole size of the grounded Cu mesh was 150 μm, which was chosen not to exceed the Debye length of the plasma. The shutter was installed above the grounded Cu mesh to control the time of film deposition by opening or closing.

To confirm the generation of any electric charge from the sputtered flux, the current flowing from the substrate holder to the ground was measured by a pico-ammeter (KEITHLEY 6487, Tektronix, Cleveland, OH, USA) during DC magnetron sputtering. Fig 2.1c shows the current measured in the substrate holder while the sputtering power was turned on. As soon as the sputtering power was turned on, a negative current of approximately − 500 μA was measured. It means that the negatively charged flux was reaching the substrate. Most would be electrons, but some would be from the negatively charged sputtered flux. The contribution from the

negatively charged sputtered flux can be identified through the bias experiment.

The DC sputtering power was varied as 20, 50, 100, and 200 W. The working pressure was varied as 2.5, 5, 10, and 20 mTorr at each sputtering power. To investigate the effect of the charged flux on the film growth, Ag films were deposited while applying the bias of−300, 0, and+300 V to the substrate holder. By varying the working pressure, sputtering power, and electric bias, Ag films were deposited under 45 different conditions. In all conditions, Ag films were deposited on a p−type Si (100) substrate for 30 min at room temperature. At the sputtering power of 200 W, the plasma was not generated at the working pressure of 2.5 mTorr. Therefore, the data at this condition is absent in d of Figs. 2.4, 2.5, 2.6, 2.7, 2.8, and 2.9 as well as in Table 2.1d.

To investigate the initial stage of deposition, sputtered Ag was deposited for a very short time of 3 seconds on an amorphous carbon membrane on the Cu grid for transmission electron microscopy (TEM). The sputtered Ag in the initial stage was observed by TEM (FEI, Tecnai F20, Hillsboro, OR, USA) operated at an accelerating voltage of 200 kV. TEM images were analyzed using the open−source software ImageJ (1.51k, National Institutes of Health, Bethesda, MD, USA).

The microstructure of the Ag films was investigated by field-emission scanning electron microscopy (FESEM) (Carl Zeiss, SUPRA, Oberkochen, Germany) operated at an accelerating voltage of 2 kV. The crystallinity of the Ag films was analyzed by X-ray diffraction (XRD) (PANalytical, X'pert-Pro, Almelo, The Netherlands) in a 2 θ scanning range of 30~80 ° with the Cu Kα (λ=1.5418 Å) source. The resistivity of the films was measured using a four-point probe (CMT-SR2000N, Materials Development Corporation).

2.3. Result and Discussion

Fig. 2.2 shows cross-section FESEM images of the Ag film deposited on a Si substrate at the sputtering power of 100 W for working pressures of 2.5 mTorr (Fig. 2.2a), 5 mTorr (Fig. 2.2b), 10 mTorr (Fig. 2.2c), and 20 mTorr (Fig. 2.2d), which had film thicknesses of 377.9, 281.3, 252, and 190.4 nm, respectively. The thickness of the Ag films increased as the working pressure decreased.

This effect of the pressure decrease is attributed to the increase of the mean free path, which results in the increase in the kinetic energy of argon ions. If the target is sputtered by argon ions with

high kinetic energy, the sputtering efficiency would increase, increasing the growth rate of films [68].

Fig. 2.1c shows that a negative current of approximately − 500 μA was measured when the sputtering power was turned on. Most of the negative current would be from electrons but there is a possibility that some of the negative current might come from the negatively charged sputtered Ag flux. To check this possibility, the Ag films were deposited for 30 min while applying biases of + 300, 0, and − 300 V to the substrate at a sputtering power of 100 W and a working pressure of 2.5 mTorr.

As shown in Fig. 2.3, the film thickness was 345.7, 377.9, and 416.0 nm for the biases of −300, 0, and +300 V, respectively. When the positive bias was applied to the substrate, the film thickness increased by 10 % whereas when the negative bias was applied to the substrate, the film thickness decreased by 8.5 %. The increase in the film thickness by the positive bias is attributed to the negatively charged flux attracted toward the substrate. Similarly, the decrease in the film thickness by the negative bias is attributed to the negatively charged flux repelled from the substrate. Although we do not know the relative percentage of positively and negatively charged fluxes, we can say that at least 8.5 % of sputtered flux is negatively charged.

Fig. 2.2 and Fig. 2.3 are representative cross-section images of all Ag films deposited under 45 different conditions. The thickness, FWHM, and resistivity of the films were measured as a function of working pressure and electric bias, and summarized in Figs. 2.4, 2.5, 2.6, 2.7, 2.8, and 2.9.

Fig. 2.4 shows how the thickness of the Ag films deposited on the electrically biased substrate depended on the working pressure at each sputtering power. The film thickness decreased with increasing working pressure at sputtering powers of 50, 100, and 200 W as shown in Fig. 2.4b, c, and d, respectively. In Fig. 2.4d, the data at 2.5 mTorr is absent as the plasma was not generated as explained in the experimental section. For the sputtering power of 20 W in Fig. 2.4a, the bias effect is not appreciable under working pressures of 10 and 20 mTorr whereas the bias effect in Fig. 2.4d is appreciable. At a low sputtering power of 20 W, most of the sputtered flux would be individual atoms. Since individual atoms have high ionization energy and low electron affinity, charging of them would be much more difficult than that of clusters or nanoparticles, which have low ionization energy and high electron affinity, approaching their work function values [69]. As a result, the bias effect would be much less at 20 W than at 200 W.

In Fig. 2.4a, however, the film thickness decreased as the

working pressure increased from 2.5 to 10 mTorr, but as the pressure increased further to 20 mTorr, the thickness did not change at 0 V but slightly increased at + 300 and − 300 V. One possible reason we can think of would be that at a low sputtering power of 20 W, the film growth rate is very low. Especially, the growth rate tends to be minimum at the working pressure of 10–20 mTorr. As the film thickness is small enough, the uncertainty is relatively large, which might be related to the insensitivity of the film thickness to the working pressure.

Generally, the thickness of the Ag films increased as the working pressure decreased. The reason would be the same as explained in Fig 2.2. Comparing Figure 2.4a–d, the film thickness increased as the sputtering power increased. For example, at the working pressure of 5 mTorr without the bias, the film thickness increased from 90.82 to 199.2, 281.3, and 536.1 nm, respectively, as the sputtering power increased from 20 to 50, 100, and 200 W. To confirm the effect of charge, the thickness of the film was compared for the three bias voltages of − 300, 0, and + 300 V for different sputtering powers and working pressures as shown in Fig. 2.5. In all sputtering powers, the thickness of the Ag films increased as the bias applied to the substrate was increased from − 300 to + 300 V. This tendency is enhanced when the working pressure is decreased. The increase in

the bias effect would be due to the increase in the mean free path with decreasing working pressure. As a result, the thickness change between biased and unbiased substrates depends on the working pressure.

Percentages of the thickness change relative to the unbiased substrate at different sputtering powers and working pressures are summarized in Table 2.1. For example, the film thicknesses are 345.7 and 377.9 nm at − 300 and 0 V, respectively, in Fig 2.3a and b at a sputtering power of 100 W and a working pressure of 2.5 mTorr, therefore, the percentage would be (345.7 − 377.9)/377.9 x 100 = − 8.52 % as shown in Table 2.1c. Except for a few cases in all conditions, the negative bias decreased the film thickness whereas the positive bias increased it. This result indicates that most sputtered flux may be neutral but some charged flux, if any, is dominantly negatively charged. If it is assumed that the positively charged flux is absent, the amount of negatively charged flux is estimated to be roughly 10 %. Generally, the thickness change increased as the working pressure decreased under all sputtering powers. It means that as the working pressure decreased, the amount of the charged Ag flux affected by the substrate bias increased, which would be due to the increase in the mean free path. At a sputtering power of 20 W in Table 2.1a, the thickness of the Ag film decreased

by 3.84 % at a working pressure of 10 mTorr and did not change at 20 mTorr. This exceptional behavior is understood clearly and the possible reason was suggested in the explanation of Fig. 2.4a.

The XRD analysis was made to study the crystallinity of the Ag films. Fig. 2.6 shows how the full width at half maximum (FWHM) on the (111) plane, which is the main pick of the Ag films, varies with the working pressure for the three bias conditions at each sputtering power. The FWHM was affected by the bias. According to the Scherrer equation, the FWHM is inversely proportional to the crystallinity [70].

$$\tau = \frac{K\lambda}{\beta \cos\theta} \qquad (2.1)$$

where τ is the mean grain size, K is a dimensionless shape factor, λ is the X-ray wavelength of Cu Kα1, β is the FWHM, and θ is the Bragg angle. Therefore, to increase the crystallinity of films, the FWHM should be decreased.

Under almost all sputtering powers and working pressures, the FWHM increased and decreased, respectively, when the bias applied to the substrate was - 300 and + 300 V. This result indicates that the crystallinity of the film increases at + 300 V and decreases at - 300 V. This means that the negatively-charged sputtered flux contributes to the increase of the crystallinity.

For the bias of − 300 V, the FWHM increased with decreasing working pressure at all sputtering powers. This would be because the repelling effect of negatively charged flux would increase with decreasing working pressure. For the bias of 0 and + 300 V, except at 2.5 mTorr, the FWHM tended to increase slightly with increasing pressure. This would be because for 0 V, the generation of the charged flux decreases with increasing pressure as mentioned before in explaining Table 2.1 and for + 300 V, the attracting effect of the negatively charged flux would decrease with increasing working pressure.

Fig. 2.7 shows how the FWHM depends on the substrate bias. In all sputtering powers, the positive and negative biases tended to decrease and increase the FWHM, respectively. The results in Fig. 2.7 indicate again that the negatively charged flux contributes to the increase of crystallinity. The bias effect is more pronounced at 200 W than at 20 W, which would come from the fact that the charged flux at 200 W would be much larger than that at 20 W.

Fig. 2.8 shows how the resistivity of the Ag films changes with the working pressure under different bias conditions at each sputtering power. The resistivity depends on the working pressure and the bias, which is similar to that of the FWHM. For the bias of − 300 V in all sputtering powers, the resistivity increased as the

working pressure decreased. However, for biases of 0 and + 300 V, the resistivity decreased as the working pressure decreased. This result indicates that the resistivity is proportional to the crystallinity.

The dependence of the resistivity of the Ag films on the bias is summarized in Fig. 2.9. In all sputtering powers, the positive bias tended to decrease the resistivity whereas the negative bias tended to increase it. This result can be explained by the contribution of the crystallinity by the charged flux as was explained for the bias effect on the FWHM.

Summarizing all the effects of sputtering power, working pressure, and electric bias results on film thickness, FWHM, and resistivity, the quality of the deposited film was improved in proportion to the amount of the charged sputtered Ag flux. Then, why does the amount of the charged flux increase as the working pressure decreases? In relation to this, Jang et al. [71] reported that the sputtering power affects the sputtered particle size, and the charging probability increases with increasing particle size because the ionization energy and the electron affinity approach the work function value as the size increases.

As the working pressure increases, the mean free path in the chamber is decreased, which increases collisions between particles. As a result, argon ions lose their kinetic energy and hit the target

with a little force. Therefore, mostly small-sized particles would be sputtered. When the working pressure decreases, however, the mean free path in the chamber increases, then argon ions are accelerated to the target with large energy with little energy loss. As a result, relatively large sputtered particles are generated.

2.4. Conclusion

The deposition behavior of Ag films was studied while changing the process parameters such as sputtering power, working pressure, and substrate bias during DC magnetron sputtering. The most important finding is that the negatively charged flux is generated during sputtering and contributes moderately to the film deposition in a way to increase the film crystallinity. The amount of the charged flux depends on the sputtering power and working pressure. The amount of the charged flux can be a new processing parameter in sputtering. The role of the sputtering power and working pressure should be understood with respect to their effect on the amount of the charged flux generated during sputtering.

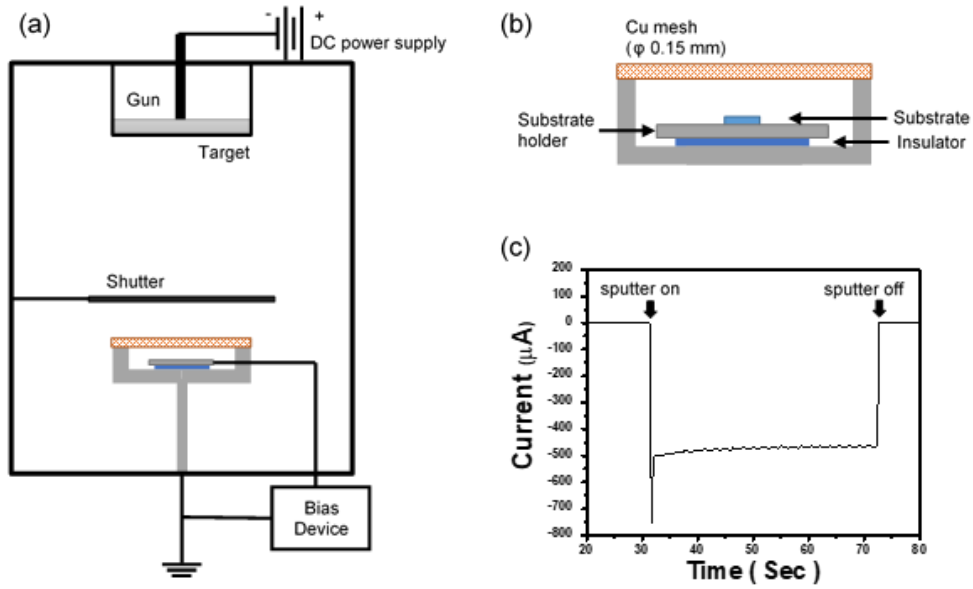

Figure 2.1 (a) Schematic of the DC magnetron sputtering chamber, (b) the substrate holder and c the current measured on the substrate holder at the plasma power of 100 W

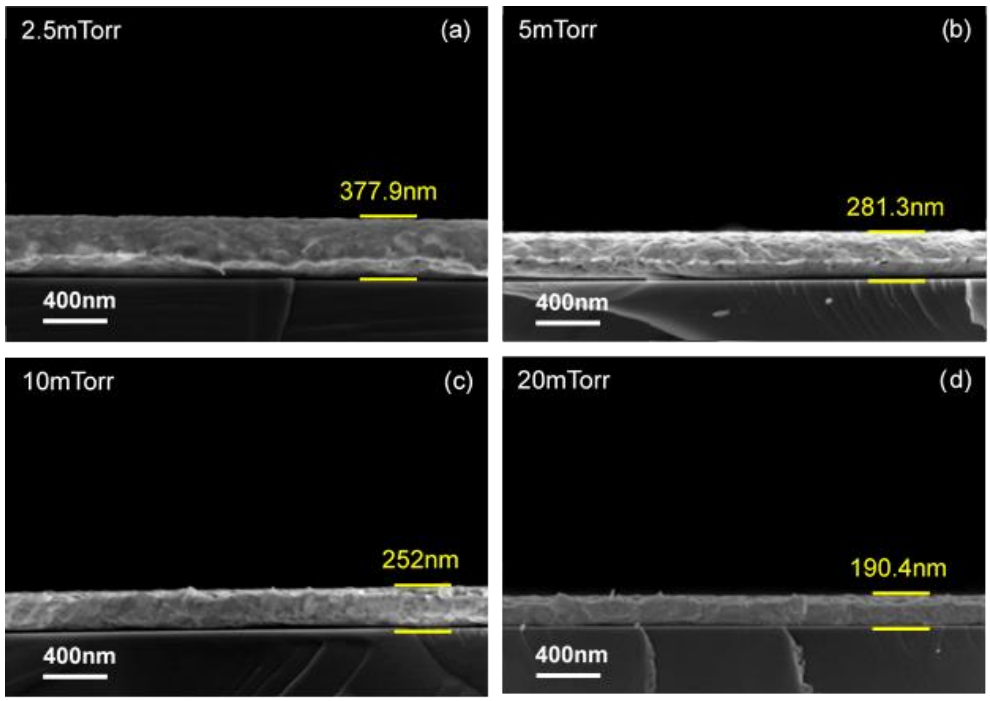

Figure 2.2 Cross-section FESEM images of the Ag films deposited on Si substrates at the working pressure of (a) 2.5 mTorr, (b) 5 mTorr, (c) 10 mTorr, and (d) 20 mTorr at the sputtering power of 100 W

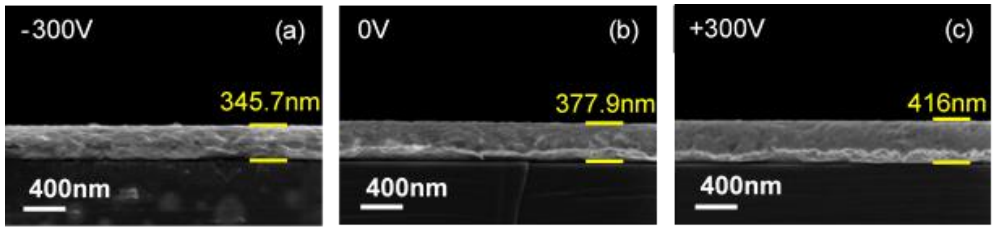

Figure 2.3 Cross-section FESEM images of the Ag films deposited on Si substrates at the electric biases of (a) −300 V, (b) 0 V, and (c) +300 V at the working pressure of 2.5 mTorr and the sputtering power of 100 W

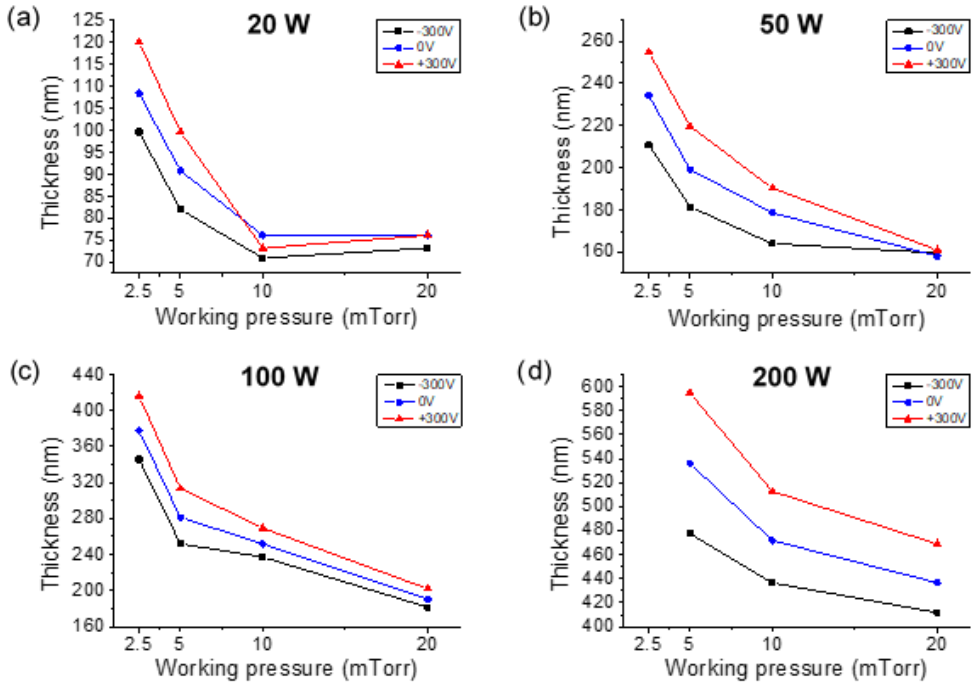

Figure 2.4 Plots of the thickness of Ag films according to the working pressure change while applying a bias to the substrate at sputtering power of (a) 20 W, (b) 50 W, (c) 100 W, and (d) 200 W

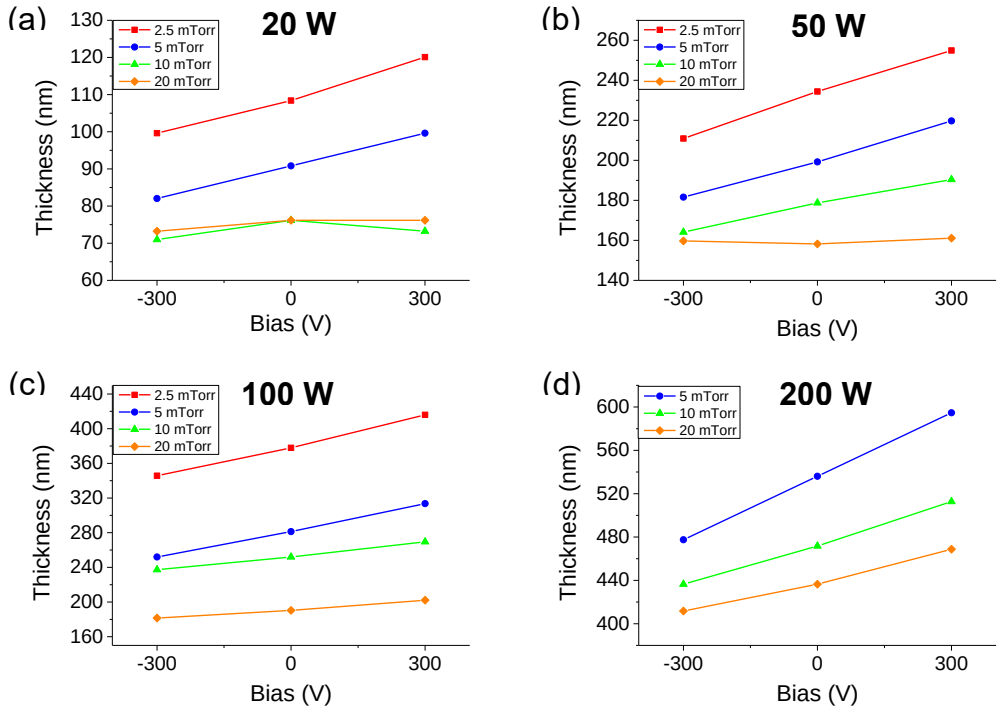

Figure 2.5 Plots of the thickness of Ag films according to the substrate bias change while changing the working pressure at the sputtering power of (a) 20 W, (b) 50 W, (c) 100 W, and (d) 200 W

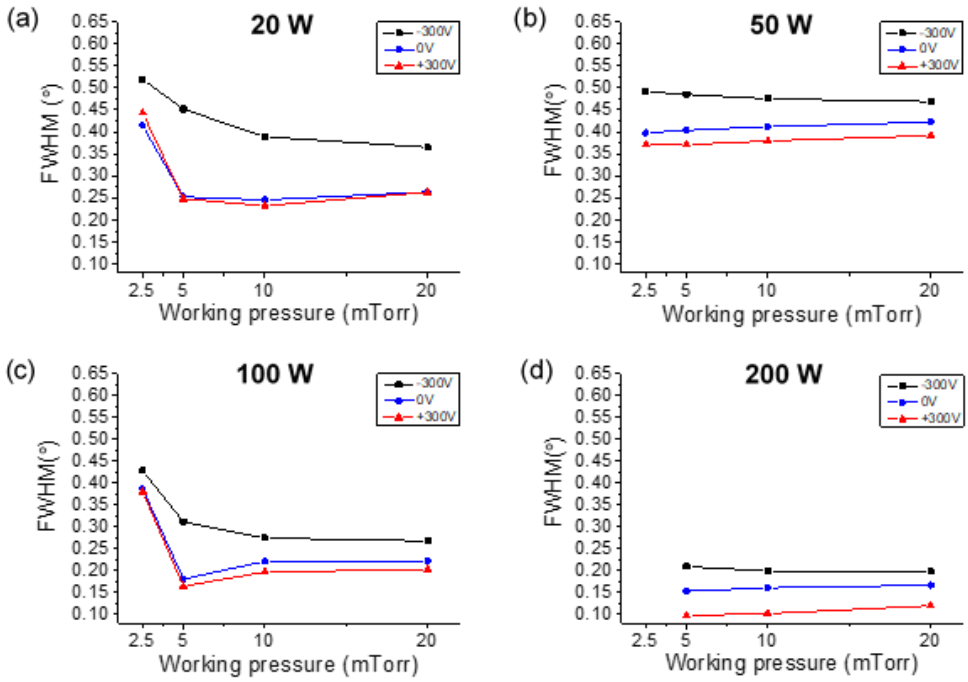

Figure 2.6 Plots of the FWHM of Ag films of (111) peak according to the working pressure change while applying a bias to the substrate at sputtering power of (a) 20 W, (b) 50 W, (c) 100 W, and (d) 200 W

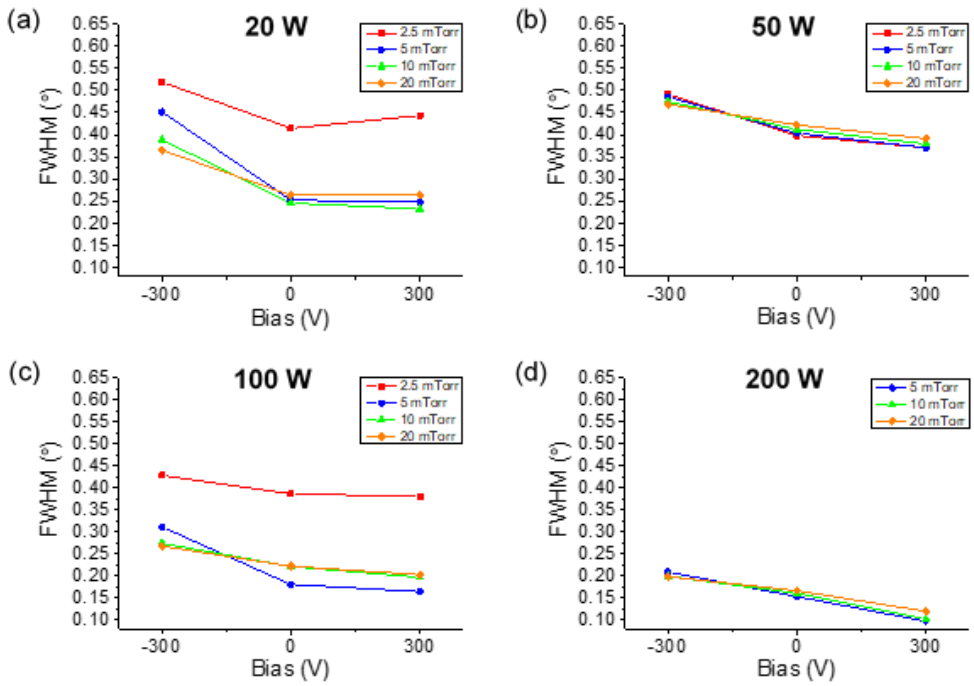

Figure 2.7 Plots of the FWHM of Ag films of (111) peaks according to the substrate bias change while changing the working pressure at the sputtering power of (a) 20 W, (b) 50 W, (c) 100 W, and (d) 200 W

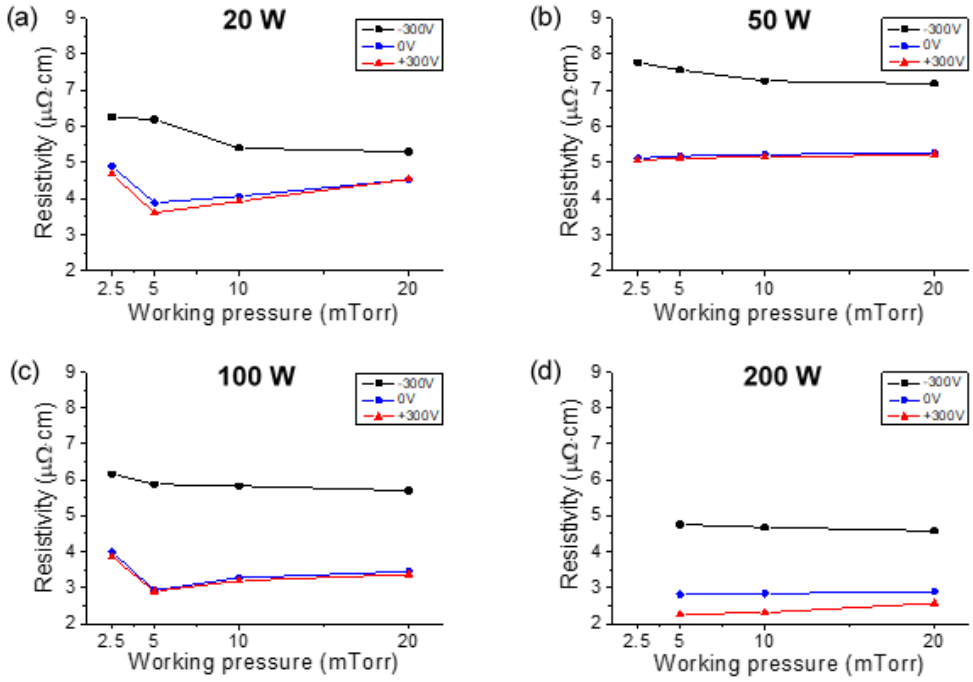

Figure 2.8 Plots of the resistivity of Ag films according to the working pressure change while applying a bias to the substrate at sputtering power of (a) 20 W, (b) 50 W, (c) 100 W, and (d) 200

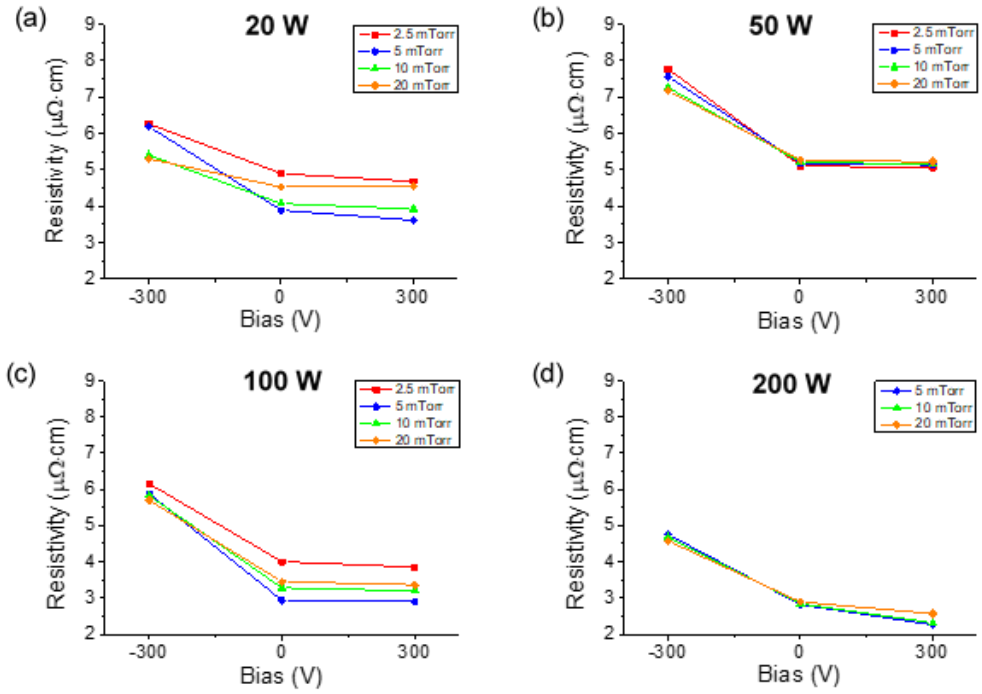

Figure 2.9 Plots of the resistivity of Ag films according to the substrate bias change while changing the working pressure at the sputtering power of (a) 20 W, (b) 50 W, (c) 100 W, and (d) 200 W

20 W	- 300 V	0 V	+ 300 V
2.5 mTorr	- 8.1	-	+ 10.7
5 mTorr	- 9.6	-	+ 9.6
10 mTorr	- 6.8	-	- 3.8
20 mTorr	- 3.4	-	0

(a)

50 W	- 300 V	0 V	+ 300 V
2.5 mTorr	- 10.0	-	+ 8.7
5 mTorr	- 8.8	-	+ 10.2
10 mTorr	- 8.1	-	+ 6.5
20 mTorr	0.9	-	+ 1.8

(b)

100 W	- 300 V	0 V	+ 300 V
2.5 mTorr	- 8.5	-	+10.0
5 mTorr	- 10.4	-	+11.44
10 mTorr	- 5.8	-	+6.9.
20 mTorr	- 4.6	-	+6.1

(c)

20 W	- 300 V	0 V	+ 300 V
2.5 mTorr	-	-	-
5 mTorr	- 10.9	-	+ 10.9
10 mTorr	- 7.4	-	+ 8.6
20 mTorr	- 5.6	-	+ 7.3

(d)

Table 2.1 Percentage of the thickness change of Ag films relative to the unbiased substrate at sputtering powers of (a) 20 W, (b) 50 W, (c) 100 W, and (d) 200W

Chapter 3. Effects of substrate bias and Ar pressure on growth of α−phase in W thin films deposited by RF magnetron sputtering

3.1. Introduction

In the recent metallization process of semiconductors, scaling of the interconnect dimension is reaching limitations and causing several problems, such as material reliability issues of copper (Cu) [73, 74]. As a replacement for Cu interconnects, tungsten (W) has been used due to its high melting point and short mean free path. Although the resistivity of W (5.3 $\mu\Omega$·cm) is higher than that of Cu (1.7 $\mu\Omega$·cm), it is predicted that the resistivity of W could be lower than that of Cu at line widths less than 25 nm [75, 76].

W exists in two major allotropes: a body-centered cubic (BCC) α-phase and a β-phase of the A-15 crystal structure [77]. Although α-phase W is thermodynamically stable, it has been reported that sputtered W films contain β-phase W [78]. The resistivity of metastable β-phase W (100~1290 $\mu\Omega \cdot$ cm) [79-81] is much higher than that of stable α-phase W (5.3 $\mu\Omega \cdot$ cm). Since the resistivity of W thin film for interconnect applications, should be close to the bulk resistivity, the fraction of α-phase W should be maximized and that of β-phase W should be minimized. Therefore, it is important to understand the underlying principles regarding the formation of α- and β-phase W.

It has been reported that β-phase W was converted to α-phase W when the sputtering power was increased [79, 82, 83], the film was deposited or annealed at high temperature [76, 79, 83], and the negative bias was applied to the substrate [79, 82, 84]. The mechanism of the phase transformation is not yet fully understood, but some researchers have suggested that the high kinetic energy of argon (Ar) ions and/or W atoms and clusters bombarding the growing surface could overcome the surface diffusion barrier and enhance the atomic diffusion [78, 85].

In this paper, we tried to identify the sputtering condition of the W film with the lowest resistivity by varying the substrate bias and

Ar pressure using a radio-frequency (RF) magnetron sputtering system. Since the low resistivity is critically related to the fraction of α-phase W, we examined the deposition parameters for the conversion from β-phase W to α-phase W. To examine the initial stage of deposition, we used a Cs-corrected mono-chromated transmission electron microscope (TEM) by which we could observe that the substrate bias had a significant effect on the amount of deposited W atoms, clusters, and nanoparticles.

3.2. Experimental

W thin films were deposited at room temperature by RF magnetron sputtering using a cylindrical chamber with a diameter of 30 cm and a height of 10 cm. The target-substrate distance was 7 cm. The W sputtering target of 10 cm in diameter has 99.95% purity. The base pressure was ~5.0×10^{-7} Torr. During sputtering, Ar gas was supplied to the chamber at a flow rate of 15 standard cubic centimeters per minute (sccm) controlled by a mass flow controller (MFC). The plasma was generated by an RF power of 60 W and a matching network of 13.56 MHz.

Substrates for W deposition were p-type silicon (100) wafers with native oxide. They were cleaned by ultrasonication in ethanol

for 10 min and dried with compressed air prior to deposition. To apply the electrical bias, the stainless-steel substrate holder was made electrically floating. To prevent the bias applied to the substrate from altering the plasma condition for sputtering, a grounded mesh with a hole size less than the Debye length [86] was installed above the substrate holder. A shutter was installed above the grounded mesh to block the sputtered flux and control the substrate exposure time.

Before the deposition, the shutter was closed for 3 min for plasma stabilization. To examine the initial stage of deposition, the shutter was opened only for 1 s. To observe the initial stage of deposition on an atomic resolution, a graphene TEM membrane of 3-5 layers was used as a substrate. For the bias experiments, the bias was applied to the stainless-steel substrate holder, which was enclosed by aluminum foil to increase the conductivity. The circular graphene membrane had a diameter of 2 mm, and the substrate holder had dimensions of 5 mm x 30 mm x 1 mm, on which the membrane was placed.

The cross-section of W thin films was analyzed by field-emission scanning electron microscope (FESEM) (SUPRA 55VP, Carl Zeiss, Oberkochen, Germany) and Cs-corrected mono-chromated TEM/scanning TEM (STEM) (Themis Z, Thermo Fisher Scientific, Waltham, Massachusetts, USA), respectively, at the

accelerating voltage of 2 kV and 300 kV. W nanoparticles deposited on the graphene membrane were also analyzed by Cs-corrected TEM at the accelerating voltage of 300 kV. The open-source software ImageJ (1.51k, National Institutes of Health, Bethesda, MD, USA) was used to analyze the size, the number density, and the percentage area of W nanoclusters and nanoparticles in TEM images. The sheet resistance of W films was measured by a 4-point probe (CMT-SR1000N, Changmin Tech, Seongnam, Republic of Korea). The grazing incidence X-ray diffraction (GIXRD) data in the 2θ range of 30 to 80 ° for analyzing the crystal structure of W thin films as well as the X-ray reflectivity (XRR) data were obtained by high-resolution X-Ray Diffractometer (HR-XRD) (X' pert Pro, PANalytical, Almelo, the Netherlands) with the Cu K-α radiation (λ=1.54 Å). The surface morphology of W films was observed by atomic force microscope (AFM) (NX-10, Park Systems, Suwon, Republic of Korea).

3.3. Results

The effect of the electric bias applied to the substrate was examined during the W film deposition. The W thin films were deposited for 10 min at an RF sputtering power of 60 W and Ar

pressure of 20 mTorr under biases of −100, 0, and +100 V applied to the substrates, as shown by the cross−section FESEM images of Fig. 3.1(a), (b), and (c), respectively. The thicknesses of the W films in Fig. 3.1(a), (b), and (c) measured by the FESEM images were 49, 70, and 62 nm, respectively.

The film deposited with the negative bias was the thinnest and that without the bias was the thickest. Fig. 3.2(a) and (b) show, respectively, GIXRD and XRR data of these films. From the GIXRD data of Fig. 3.2(a), the phase of the W films could be identified. The β−phase W peaks indicating the (200), (211), (320), and (321) planes were shown under all bias conditions, but the α−phase W peaks indicating the (200) and (211) planes were shown only at the substrate bias of −100 V. Moreover, the peaks of the β phase were broadened under the positive bias, implying that the film should have a nanocrystalline or an amorphous−like structure. The resistivities of these films were 157 ± 8, 699 ± 85, and 2723 ± 228 $\mu\Omega \cdot$cm at the substrate biases of −100, 0, and +100V, respectively, as shown in Table 2.1. The resistivity increased as the bias changed from −100 to +100 V.

In agreement with the XRD data in Fig. 3.2(a), the film deposited with the bias of +100 V had the highest resistivity, which was attributed to electron scattering at the grain boundaries enhanced by

the nanocrystalline or an amorphous-like structure, as shown later in Fig. 3.9. In addition, the critical angle of each film was determined by XRR data, and the density was calculated by the following equation [87]:

$$\frac{{\theta_c}^2}{\rho} = \frac{r_e \lambda^2 Z N_A}{\pi \mathrm{A}} = \mathrm{B}, \qquad (3.1)$$

where θ_c is the critical angle, r_e is the classical electron radius (2.82×10^{-15} m), λ is the X-ray wavelength, Z is the atomic number, N_A is Avogadro's number, and A is the mass number. At the substrate biases of -100, 0, and +100 V, the critical angles were, respectively, 0.52, 0.45, and 0.41 with calculated densities of 16, 12, and 10 $\mathrm{g/cm^3}$, respectively.

The bias effect would be affected by Ar pressure on which the mean free path depends. The bias experiments were done with Ar pressure varying from 5 mTorr to 80 mTorr. The properties of W films deposited under the bias with varying Ar pressure are indicated in Table 2.1. Under all Ar pressures, the W films deposited at the negative substrate bias had a higher density and lower resistivity than those of the other bias conditions. The lowest resistivity of the W film was achieved under 80 mTorr and at the substrate bias of -100 V.

To understand why the W film deposited under 80 mTorr and the

substrate bias of −100 V had the lowest resistivity, the films deposited under the bias of −100 V and different Ar pressures, of 5, 20, 45, and 80 mTorr, were analyzed by XRD, as shown in Fig. 3.3. As the pressure increased from 5 to 80 mTorr, the XRD intensities of the β−phase W peaks decreased and those of the α−phase W peaks increased. Under 80 mTorr, the α−phase W thin film was deposited. The lowest resistivity of the film deposited under 80 mTorr seemed to come from its highest fraction of α−phase W.

Not only the fraction of α−phase W but also the surface morphology of the film affected film resistivity. Fig. 3.4 shows the surface morphologies of films deposited under 80 mTorr where the bias effect was most pronounced. As the substrate bias changed from −100 to +100 V, the grain size decreased, and the roughness increased from 0.4 to 0.6 and 0.9 nm. As the grain size decreased and the roughness increased, the resistivity of the thin film increased due to the scattering of electrons [88].

To examine the behavior of the charged W flux in the initial stage of film deposition, we deposited only for 1 s by opening the shutter for 1 s and then closing it. The high−conductivity graphene membrane of 3−5 layers was used for TEM observation, and the electric bias was applied to the substrate holder on which the graphene membrane was placed. Fig. 3.5 (a)−(c) shows the high

angle annular dark field (HAADF)−STEM images of the W flux deposited on the graphene membrane for 1 s. The number density and size of nanoparticles changed with the substrate bias condition. The size and frequency of nanoparticles are illustrated in Fig. 3.6 (a). Only nanoparticles larger than 1.25 nm were counted because nanoparticles smaller than 1.25 nm were too small to be distinguished by image contrast. Instead, the percentage areas of nanoparticles smaller than 1.25 nm per 25×25 nm2 were analyzed, as illustrated in Fig. 3.6(b). Hereafter, we refer to the nanoparticles smaller than 1.25 nm as nanoclusters. The number densities of nanoparticles were 184, 146, and 98 per 100×100 nm2 for the substrate biases of −100, 0, and +100 V, respectively. The size distribution became broader and the average particle size increased from 2.47 to 2.79 and 3.09 nm as the bias was changed from −100 to 0 to +100 V. The percentage areas of nanoclusters were 10, 7, and 6 % for the substrate biases of −100, 0, and +100 V, respectively. As the bias changed from +100 to 0 to −100 V, the number of nanoparticles and the number of nanoclusters both increased, indicating that some of them were positively charged.

HRSTEM images with the fast Fourier transformation (FFT) images of W nanoparticles are shown in Fig. 3.5(d)−(f). Nanoparticles, nanoclusters, and a few atoms were observed. The

lattice fringe of nanoclusters was hardly observed because they were amorphous. However, the lattice fringe of nanoparticles larger than 1.25 nm could be observed and they were analyzed by the FFT images to be β-phase W, as shown in the inset lower right of Fig. 3.5(d)-(f). When the size was very small, the amorphous phase was stable, and when the size was larger than 1.25 nm, the β phase was stable, indicating that the size of W particles was related to their phase.

The XRD data in Fig. 3.2(a) show that the W films deposited with the negative bias consisted of α- and β-phases. However, the STEM images in Fig. 3.5(d) show that all W nanoparticles consisted only of β-phase in the initial stage of deposition with the negative bias. Considering these results, it seems that β-phase W was formed first and transformed to α-phase W when the bias of -100 V was applied.

To examine the formation of α-phase W, we deposited W films for only 3 min under the biases of -200, -100, 0, and +100 V. The films were analyzed by XRD, as shown in Fig. 3.7(a). Peaks of α-phase W were observed only in the film deposited under the bias of -200 V. It should be noted that the relative peak intensity of α-phase W in the film deposited for 3 min under the bias of -200 V (Fig. 3.7(a)) was stronger than that of α-phase W in the film deposited

for 10 min under the bias of −100 V (Fig. 3.2(a)). This result indicates that the negative bias had a strong effect on the formation of α−phase W. The thicknesses of films deposited under the biases of −200, −100, 0, and +100 V were, respectively, 13, 16, 18, and 17 nm.

Fig. 3.7(b) shows their growth rates. The film thickness increased as the bias changed from −200 to 0 V and then decreased as the bias changed from 0 to +100 V, showing a tendency similar to those in Fig. 3.1 and Table 3.1. The resistivities of the films deposited under the biases of −200, −100, 0, and +100 V were, respectively, 115 ± 2, 168 ± 2, 378 ± 2, and 1894 ± 43 $\mu\Omega$ · cm, as shown in Fig. 3.7(b). The resistivity increased as the bias changed from −200 to +100 V, showing a similar tendency to that of Table 3.1.

To analyze the microstructure of these films in more detail, W films deposited for 3 min at the biases of −200, 0, and +100 V were observed by TEM. As shown in Fig. 3.8(a), both α−phase and β−phase W existed in the film at the bias of −200 V. The red square area on the left of the film, which is magnified in Fig. 3.8(b), was single crystalline, as revealed by the lattice fringe. The FFT image of this square area in Fig. 3.8(b) indicates the single crystalline α−phase W with the (011) and (112) planes along the <311> zone axis.

The red square area on the center of the film, which is magnified in Fig. 3.8(c), was not single crystalline. The left side of this area in Fig. 3.8(c) shows the extension of the crystalline lattice of α-phase W, which had d-spacing of 0.22 nm. Although this lattice did not continue, the other lattice, which had d-spacing of 0.26 nm, was also observed, indicating the (002) plane of β-phase W. The FFT image of this square area in Fig. 3.8(c) indicates the mixture of α-phase and β-phase W. The red square area on the right of the film, which is magnified in Fig. 3.8(d), was nanocrystalline β-phase W with the (002) and (102) planes, which had d-spacing of 0.26 and 0.23 nm, respectively. The FFT image of this square area in Fig. 3.8(d) indicates nanocrystalline β-phase W.

The interesting aspect of the cross-sectional HRTEM image of -200 V is the formation of the amorphous W-Si layer between the native oxide layer and the Si wafer, as shown in Fig. 3.8(a). This layer was ~2 nm and ~1 nm thick, respectively, under the biases of -200 and -100 V. However, the layer was not formed in the film deposited under the bias of 0 and +100 V. It is surprising that W underwent diffusion across the native oxide layer at room temperature. One possibility is that the positive W flux should be accelerated toward the substrate by the negative bias, bombarding the surface. This bombardment might be related to the W diffusion

across the native oxide layer at room temperature.

At the bias of 0 V, the film consisted fully of β−phase nanocrystalline W, as revealed by the TEM image and FFT patterns in Fig. 3.9(a). At the bias of +100 V, most of the film was amorphous and some of the film was β−phase W, as revealed by the TEM image and FFT patterns in Fig. 3.9(b). These results of TEM and FFT images are consistent with the XRD data of Fig. 3.7(a).

To investigate the effect Ar pressure on the amount of charged W flux generated during sputtering, the deposition experiment was conducted under 80 mTorr. Fig. 3.10 shows HAADF−STEM images of the W flux deposited on the graphene membrane for 3 s at the substrate biases of (a) −100, (b) 0, and (c) +100 V. The percentage areas of nanoclusters or nanoparticles were about 18, 12, and 2 for the substrate biases of –100, 0, and +100 V, respectively, as shown in Fig. 3.11. Consistent with the experimental results at 20 mTorr, both the number of nanoparticles and nanoclusters increased as the bias was changed from +100 to 0 to –100 V. However, the magnitude of the change was greater in the experiment at 80 mTorr.

3.4. Discussion

Fig. 3.1 shows that the W film deposited under the biases of −

100 V and +100 V was thinner than that deposited under the bias of 0 V. In addition, as shown in Table 3.1, the growth rate of the film deposited under the bias of 0 V was approximately twice that of the film deposited under the bias of +100 V at 80 mTorr. Furthermore, the growth rate of the film deposited under the 0 V bias was approximately 1.45 times that of the film deposited under the −100 V bias at 20 mTorr. In relation to these results, Kim et al. [89] reported a similar bias effect on the growth rate of titanium films during RF sputtering. To explain the bias effect, they suggested that the sputtered flux became positively charged via collision with Ar ions and other positively charged species and that the amount of the positively charged flux increased with increasing Ar pressure because the collision frequency increased.

Applying Kim et al.' s suggestion [89] to our result, the positively charged W flux was formed by collisions with the positive sources in the gas phase, and they were repelled from the substrate with the +100 V bias. The growth rate of the film decreased compared to that deposited under the 0 V bias, as shown in Fig. 3.1 and Table 3.1. Also, the difference in the amount of W nanoparticles deposited at biases of −100 V and +100 V was significant under 80 mTorr, as shown in Fig. 3.10, compared to under 20 mTorr, as shown in Fig. 3.5. When Ar pressure increased from 5 mTorr to 80 mTorr,

the mean free path decreased and the collision frequency increased, and a higher fraction of the W flux became positively charged. Therefore, the bias effect on the growth rate of the film increased as Ar pressure increased.

This leads to the question of why the negative bias decreased the film growth rate in Fig. 3.1 and Table 3.1. The following potentially explains this result. The negative bias attracts and accelerates the positive flux. Some of the accelerated positive flux including Ar ions might resputter the film by bombarding the surface with high-incident energy. This might explain the growth rate of the film on the negatively biased substrate decreasing compared to that deposited under the 0 V bias.

When the negative bias was applied to the substrate, the resistivity of films decreased under all pressure conditions, as shown in Table 3.1. The resistivity decrease is mainly attributed to the formation of α-phase W, which is confirmed by the GIXRD data in Fig. 3.2(a), Fig. 3.3, and Fig. 3.7(a). This leads to the question of why the negative bias induced the formation of α-phase W. Previously, Petroff et al. [79] reported that the flux of oxygen ions reached the substrate less under negative bias than under the zero or positive biases. Because β-phase W is stabilized in the presence of oxygen, the low oxygen content contributed to the formation of

α−phase W. Vullers et al. [82] explained that Ar ions and charged W species were attracted to the negatively biased substrate bombarding the thin film. Therefore, the thermal energy of the thin film increased, and the W ions with high kinetic energy were implanted. The increased thermal energy and implanted high−energy ions resulted in the atom migration to stable α−phase W.

In our study, the formation of α−phase W was improved as the negative bias increased from −100 to −200 V, as shown in Fig. 3.7(a). Considering previously reported explanations, it is probable that the negative electric field between the grounded mesh and the substrate holder accelerated the positively charged flux and that hence the kinetic energy of charged species increased. The kinetic energy likely increased as the negative bias increased from −100 to −200 V. Therefore, the bombardment of the charged flux with the film surface would transfer the kinetic energy to deposited W atoms and induces the atomic diffusion. Furthermore, the result of a three−dimensional Monte Carlo simulation conducted by Torre et al. [90] showed that the tantalum film deposited by energetic particles during sputtering was denser and smoother than that deposited without energetic particles. This result agrees with the increase in the film density in Table 3.1 and the decrease in the surface roughness in Fig. 3.4, when the bias of −100 V was applied to the substrate.

However, the increase in the fraction of α-phase W with increasing Ar pressure could not be explained by the kinetic-energy-assisted diffusion, because the bombardment energy would decrease with increasing pressure due to the decrease in the mean free path. One possible explanation for the pressure effect is charge-enhanced kinetics [59]. This possibility was first suggested to explain that charged nanoparticles can be the building blocks of thin film growth, for which charged nanoparticles should be liquid-like or superplastic. Recently, the notion of charge-enhanced kinetics has been experimentally confirmed in many experiments [16, 91, 92]. Below, we explain the increase in the fraction of α-phase W with increasing Ar pressure based on charge-enhanced kinetics.

In the initial stage of deposition, very small amorphous nanoclusters and β-phase W nanoparticles larger than 1.25 nm were formed on the substrate, as shown in Fig. 3.5. It is quite clear that as the size of W particles increases, α-phase W becomes more stable than β-phase W, although we cannot determine the exact size at which the stability is reversed. Even if the size of the W particles or the thickness of the W thin film is large enough for the stability reversal, β-phase W cannot be transformed to α-phase W because of the kinetic barrier. This aspect is evident in Fig. 3.2(a), where β-phase W films were deposited under the biases of 0 and

+100 V, despite the thickness being greater than that under the bias of −100 V. In this situation, the transformation of β−phase W to α−phase W can be triggered by charge−enhanced kinetics. For this to happen by applying the negative bias to the substrate, positive charges must build up on the film surface. Therefore, we need to explain how positive charges build up when the pressure increases.

As the pressure increased, the collision frequency of sputtered W with Ar ions or other positively charged species increased. As a result, the percentage of the positively charged W flux increased. When the negative bias was applied to the substrate, the positively charged W flux was attracted to the silicon substrate with the thin layer of native silicon oxide, and the positive charges would build up on the substrate. In addition, the built−up charges would trigger the transformation from β−phase W to α−phase W.

On the other hand, the W−Si layer was formed below the layer of native silicon oxide, as shown in Fig. 3.8(a). The formation of the W−Si layer was not observed under the zero or positive biases but was observed under the negative bias. This result indicates that W atoms must have diffused across the layer of native silicon oxide. Considering that during RF sputtering, the substrate temperature, which was estimated by the K−type thermocouple installed in the substrate holder, was maintained at ~ 20℃, it is very difficult to

explain the diffusion of W atoms across the layer of native silicon oxide at such low temperature. Therefore, the formation of the W-Si layer is another indication that the diffusion of W atoms was enhanced by the build-up of positive charges on the negatively biased substrate.

3.5. Conclusion

W thin films were deposited under various pressures and different substrate biases. As Ar pressure increased, the resistivity of W films decreased, accompanied by the formation of α-phase W. The formation of the W-Si layer, which was observed on the negatively biased substrate, indicated that the building up of positive charges on the substrate enhanced the diffusion of W atoms across the layer of native silicon oxide at room temperature. Such kinetic enhancement by charges appears responsible for the formation of α-phase W with low resistivity on the negatively biased substrate.

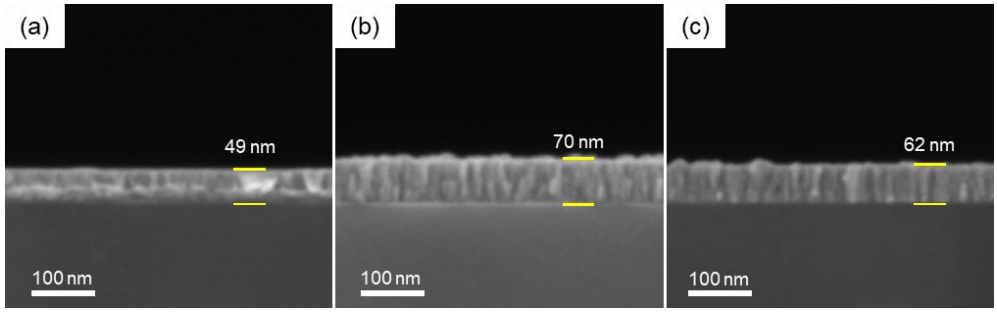

Figure 3.1 FESEM images of W films deposited on Si substrates under 20mTorr at the substrate biases of (a) −100, (b) 0, and (c) +100 V

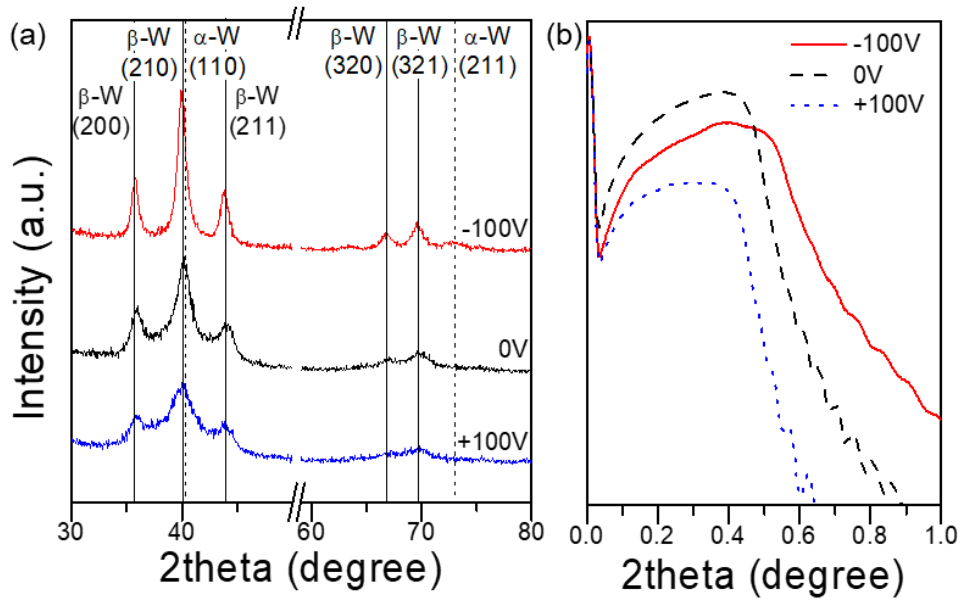

Figure 3.2 (a) GIXRD and (b) XRR data of W films deposited under 20 mTorr at the substrate biases of −100, 0, and +100 V

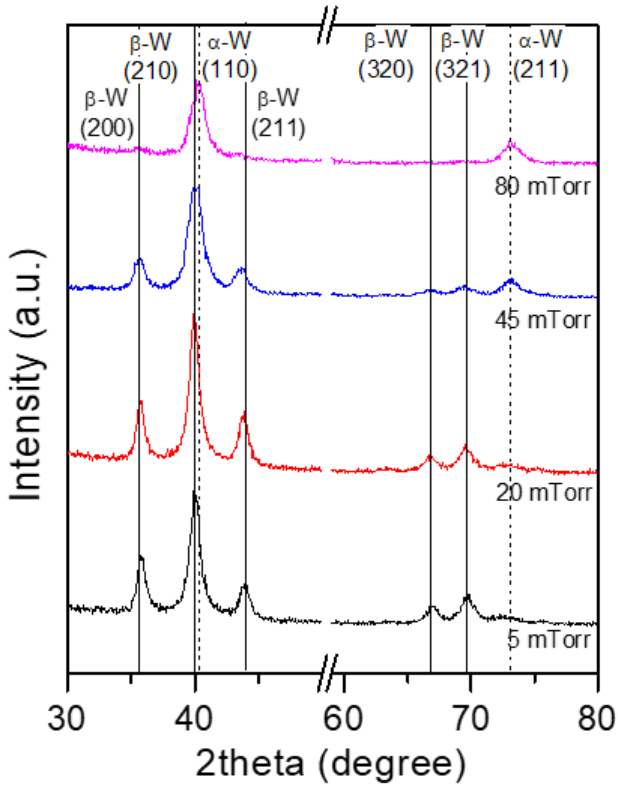

Figure 3.3 GIXRD data of W films deposited under the substrate bias of −100 V and Ar pressures of 5, 20, 45, and 80 mTorr

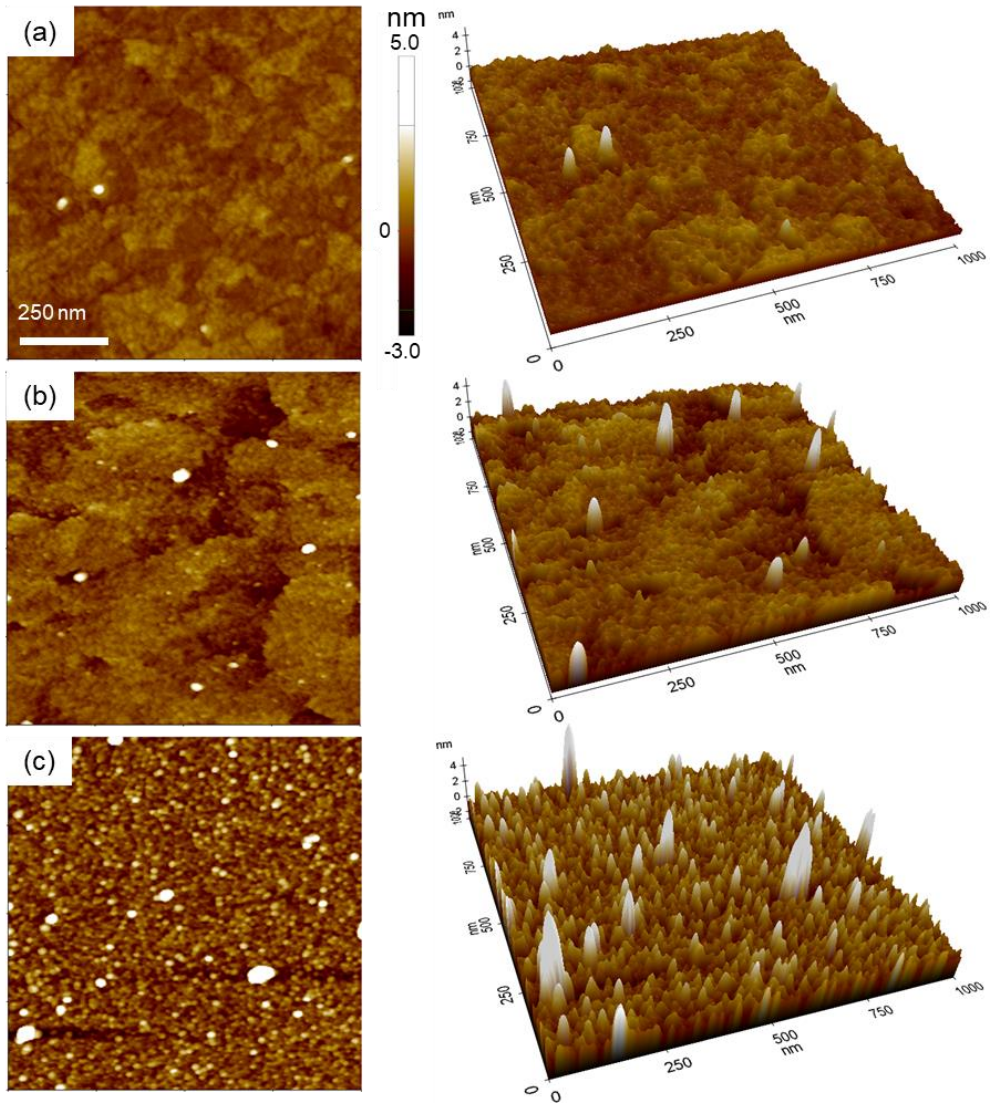

Figure 3.4 AFM surface morphologies of W films deposited under 80 mTorr at the substrate biases of (a) −100, (b) 0, and (c) +100 V

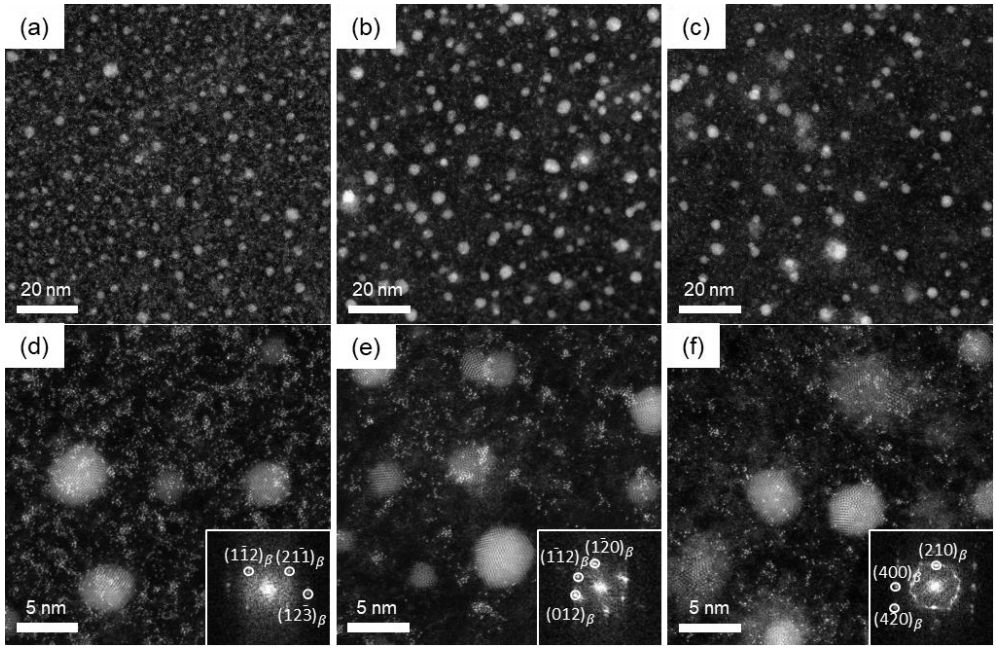

Figure 3.5 HRSTEM images of captured W nanoparticles on 3–5 layers graphene membranes at the substrate biases of (a) −100, (b) 0, and (c) +100 V. (d), (e), and (f) are high magnification STEM images of (a), (b), and (c), respectively, with FFT information (inset of the lower right in the image)

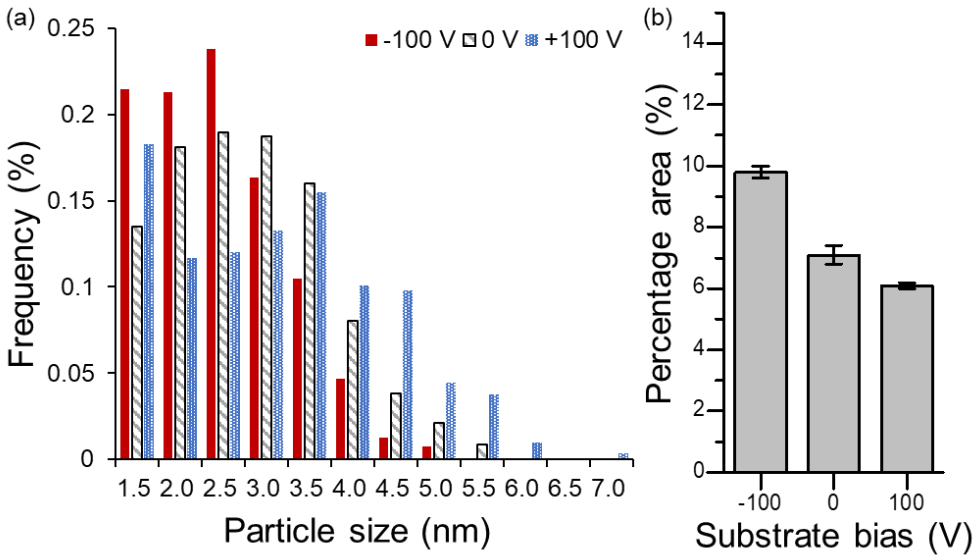

Figure 3.6 (a) The particle size distribution of nanoparticles larger than 1.25 nm and (b) The percentage area of nanoclusters smaller than 1.25 nm determined from the STEM images in Figure 3.5

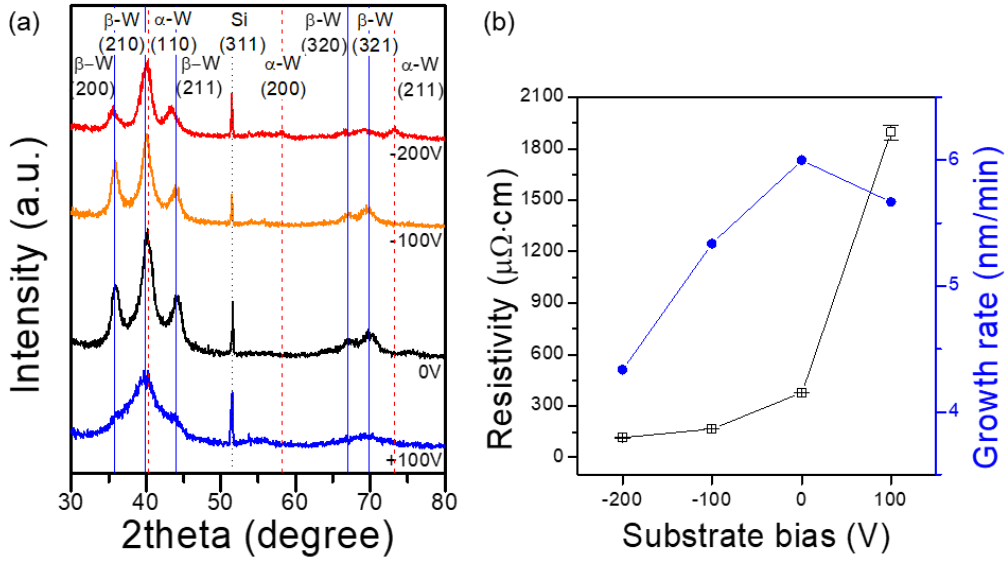

Figure 3.7 (a) GIXRD data of W films deposited for 3 min at the substrate biases of −200, −100, 0, and +100 V. And (b) The dependence of the resistivity and growth rate of films on the substrate bias

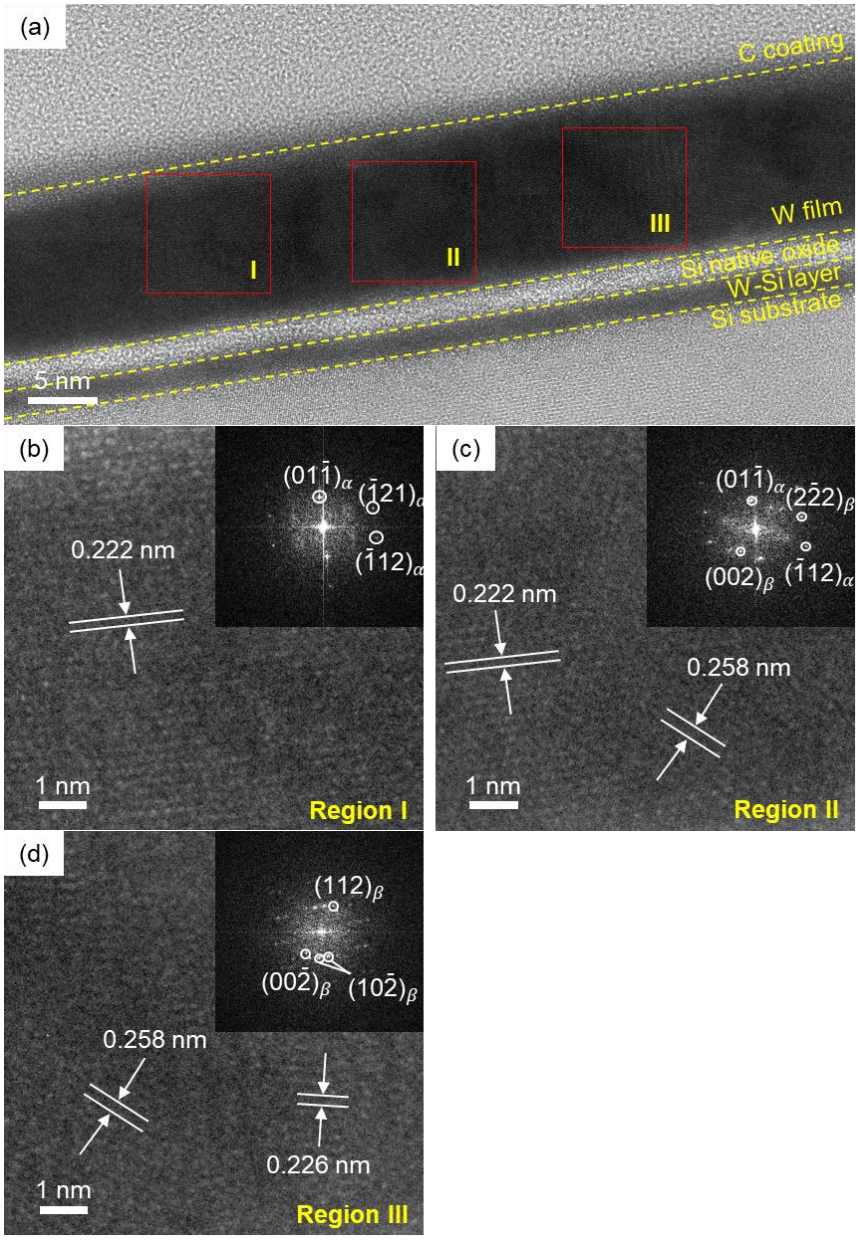

Figure 3.8 (a) Cross-sectional HRTEM of W films deposited for 3 min at the substrate bias of −200 V. (b-d) Magnified images and FFT information (inset of the upper right in the image) of (b) region I, (c) region II, and (d) region III indicated by red squares in (a)

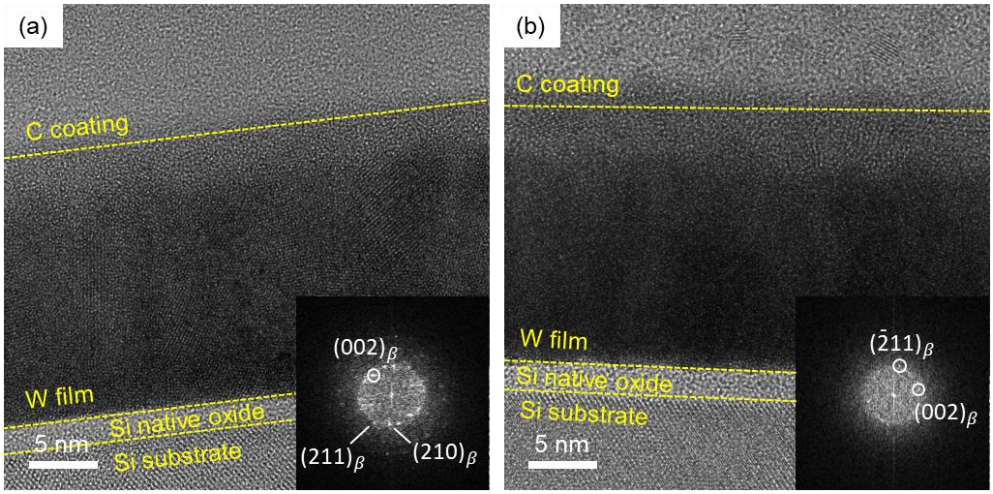

Figure 3.9 Cross-sectional HRTEM images with FFT information (inset of the lower right in the image) of W films deposited for 3 min at the substrate biases of (a) 0 and (b) +100 V

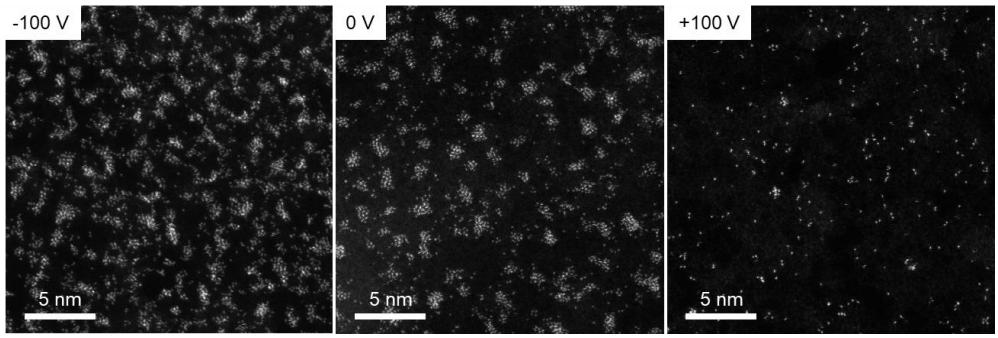

Figure 3.10 HRSTEM images of captured W nanoparticles for 3 sec under 80 mTorr on multi layers graphene membranes at the substrate biases of (a) −100, (b) 0, and (c) +100 V.

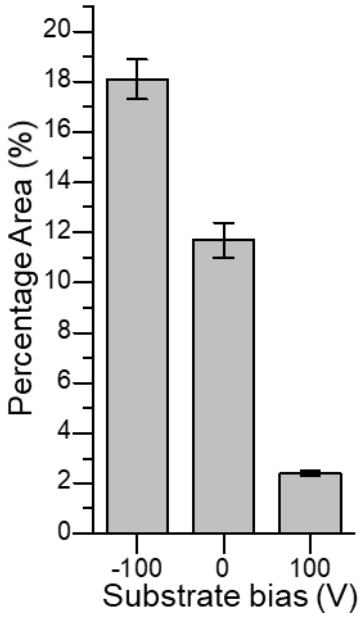

Figure 3.11 The percentage area of nanoclusters and nanoparticles determined from the STEM images in Figure 3.10

Ar pressure (mTorr)	Substrate bias (V)	Deposition time (min)	Thickness (nm)	Growth rate (nm/min)	Resistivity (μΩ cm)	Density (g/cm^3)
5	-100	10	58	5.8	149 ± 9	17
	0	10	68	6.8	245 ± 16	17
	+100	10	69	6.9	278 ± 49	15
20	-100	10	49	4.9	157 ± 8	16
	0	10	70	7.0	699 ± 85	12
	+100	10	62	6.2	2723 ± 228	10
45	-100	10	40	4.0	75 ± 19	17
	0	10	46	4.6	412 ± 69	14
	+100	10	38	3.8	6818 ± 746	9
80	-100	15	28	1.9	38 ± 4	16
	0	15	32	2.1	128 ± 8	14
	+100	35	37	1.1	10351 ± 1100	-

Table 3.1 Properties of W films deposited at different Ar pressures and substrate biases

Chapter 4. Effects of substrate bias and Ar pressure on growth of α-phase in W thin films deposited by RF magnetron sputtering

4.1. Introduction

Tungsten (W) is a transition metal, which has the high melting point (3693 K), high density (19.3 g/cm^3) [93]. In addition, tungsten has high hardness and excellent ductility. Because of these characteristics, W has been widely used in various applications such as bullets for military purposes, radiation beam collimators for medical instruments, and incandescent light bulb.

In addition, W thin films are also used in metallization process of semiconductors. As semiconductor devices have been miniaturized, the line width of copper interconnects currently used has also decreased, causing problems such as resistivity size effect [94]. Therefore, W, which has a shorter electron mean free path than copper, is used instead of copper to reduce the resistivity size effect.

W has two kinds of atomic arrangements. Fig. 4.1 shows the

crystal structure of (a) α-W, which has a body-centered cubic structure and (b) β-W, which has an A-15 equiaxed crystal structure. α-W is the most stable structure and has very low resistivity.

In the previous results in Chapter 3, we discussed that the sputtered W flux was positively charged by collision with ionized Ar. Furthermore, the α-W thin film of low resistivity could grow as the pressure increased from 20 to 80 mTorr. In other words, the growth of α-W was influenced by the ionization rate. It was reported that ionization fraction of sputtered material was 10 % during DC sputtering[95]. Because of low ionization rate of DC sputtering system, RF sputtering was introduced and have replaced DC sputtering for thin film deposition.

In this study, inductively coupled plasma (ICP) was introduced to the DC sputtering system to increase the ionization density during DC sputtering. While increasing the ICP power, it was confirmed whether ICP contributed to the growth of alpha-tungsten and the decrease in film resistivity.

4.2. Experimental

Fig. 4.2 is a schematic of a DC magnetron sputtering system

assisted by ICP. A shutter was installed above the grounded mesh to block the sputtered flux and control the substrate exposure time. Before the deposition, the shutter was closed for 3 min for plasma stabilization. A three-turn ICP antenna was mounted on the magnetron, DC power was applied to the magnetron, and 13.56 MHz RF power was applied to the ICP antenna to generate the plasma in front of the magnetron.

Prior to the experiment, the sputtering chamber was evacuated to be less than 5×10^{-6} Torr. DC power was kept at 200 W and ICP power was varied from 50 to 200 W. To keep the amount of gas flow during sputtering, the flow rate of Ar gas was controlled by a mass flow controller (MFC). Substrates for W deposition were p-type silicon (100) wafers with native oxide. A grounded mesh was installed above the substrate. With this grounded mesh, which had the hole size less than the Debye length of the plasma [86], the electrical potential of the substrate did not interfere with the plasma. Thus, the same plasma condition could be maintained regardless of the electrical potential generated by the substrate bias.

The cross-section of W thin films was analyzed by field-emission scanning electron microscope (FESEM) (SUPRA 55VP, Carl Zeiss, Oberkochen, Germany) at the accelerating voltage of 2 kV. The sheet resistance of W films was measured by a 4-point

probe (CMT-SR1000N, Changmin Tech, Seongnam, Republic of Korea). The grazing incidence X-ray diffraction (GIXRD) data in the 2θ range of 30 to 80 ° for analyzing the crystal structure of W thin films was obtained by high-resolution X-Ray Diffractometer (HR-XRD) (X' pert Pro, PANalytical, Almelo, the Netherlands) with the Cu K-α radiation (λ=1.54 Å). The surface morphology of W films was observed by atomic force microscope (AFM) (NX-10, Park Systems, Suwon, Republic of Korea).

4.3. Result and Discussion

The effects of the electric bias applied to the substrate and ICP power on the W film deposition were examined during DC sputtering. The substrate bias was varied from −200 to 0, and +200 V and ICP power was increased from 0 to 200 W. Figure 4.3 shows the resistivities of these films. Under all ICP power conditions, the resistivity was lower at −200 V than 0 V. Under 100 and 200 W ICP power conditions, the resistivity was higher at +200 V than 0 V. However, the resistivity was the highest at 0 V with no ICP power. In addition, the resistivity was the highest with no ICP power under all bias conditions. As the ICP power increased from 0 to 200 W, the resistivity decreased except for the bias condition of −200 V.

Although there were some exceptions, there was the tendency that the resistivity decreased with negative bias and high ICP power. As the ICP power increased, the amount of ionized Ar gas increased.

To examine the exception under the bias of −200 V that the resistivity of film was higher under ICP power of 200 W than of 100 W, the phase of film was identified by GIXRD data. This is because that the difference in the resistivity of films might be related to the phase. The resistivity of films would increase as the phase fraction of β−W to α−W increases because the resistivity of β phase W is much lower than that of α phase W. In addition, W films deposited under ICP power of 50 and 150 W was examined to analyze the tendency more specifically. Figure 4.4 shows the GIXRD data of W films under various ICP powers of 0, 50, 100, 150, and 200 W. As ICP power increased from 0 to 100 W, the intensity of β−W GIXRD peaks decreased and that of α−W peaks increased. On the other hand, GIXRD data of W films deposited under ICP powers of 100, 150, and 200 W was very similar. These results show that the phase−dependent resistivity change of W films is only up to 100 W, and there is no phase−dependent change beyond that.

The other factor that affected the film resistivity is the grain size. As the grin size decreased and the amount of grain boundary increased, the number of electrons scattered in the grain boundary

increased. Figure 4.5 shows the morphologies of W films obtained by AFM. Under ICP powers of 0 and 50 W, the grain size was very small. Under 100 W, the grain size was the largest. Under 150 and 200 W, the grain size was smaller than that of under 100 W, but they appeared to be self-assembled.

From all these results, it seemed that the resistivity of W films was related to the phase of W and the grain size. It should be discussed how ICP power affected the W phase and the grain size. Setsuhara et al. [96] investigated the density of electrons depending on ICP power using aluminum (Al) target. The magnetron target voltage was fixed at −200 V, and the power of the ICP antenna was increased from 0 to 400 W. The application of the RF power of 100 W to the ICP antenna in addition to the DC power to the magnetron in this magnetron system significantly enhanced the electron density by two orders of magnitude compared to no assisted ICP power. As increasing ICP power from 100 to 400 W, the electron density increased more but the magnitude of the increase decreased. This result show that the plasma characteristic changed drastically upon introduction of ICP, even at low power.

As ICP power increased, the number of ionized Ar and electrons increased drastically. When sputtered W flew across the plasma, they would more collide with Ar ions with increasing ICP power. Because

Ar is an inert gas, the ionization energy of Ar is much higher than any metal. In other words, when sputtered W collided with ionized Ar, they would be charged positively, losing electrons to Ar. There are recent studies on charge enhanced kinetics. As the ratio of charged flux to neutrals increase, deposited W films transformed to α phase, which is stable phase, by charge enhanced kinetics. Furthermore, the grain size increased because atomic diffusion also enhanced.

Sahu et al. [97] studied the electrical properties of the films deposited with the variation of ICP power. The carrier concentration and Hall mobility of the films were increased as ICP power increased from 0 to 250 W and slightly decreased with increasing ICP power. Corresponding to this result, the film resistivity increased with increasing ICP power from 0 to 250 W and decreased with increasing ICP power from 250 to 400 W. Considering this result, there might be limitation that charged flux enhanced electrical property of film. From the substrate bias experiment result, sputtered W flux appeared to be positively charged. When the ratio of positively charged flux to neutral flux further increased, the mobility of electrons in film might slow be slow because of the lack of electrons.

4.4. Conclusion

W thin films were deposited by DC magnetron sputtering system assisted by ICP. When the power of ICP increased from 0 to 200 W, the resistivity of film decreased. In addition, the resistivity decreased when the negative bias was applied to the substrate. However, when the substrate bias of −200 V was applied, the resistivity increased with increasing ICP power from 100 to 200 W. This result showed that there might be a saturation point of charge−enhancing effect. As a result, 100 W of ICP power was the best condition for depositing low−resistivity α phase W.

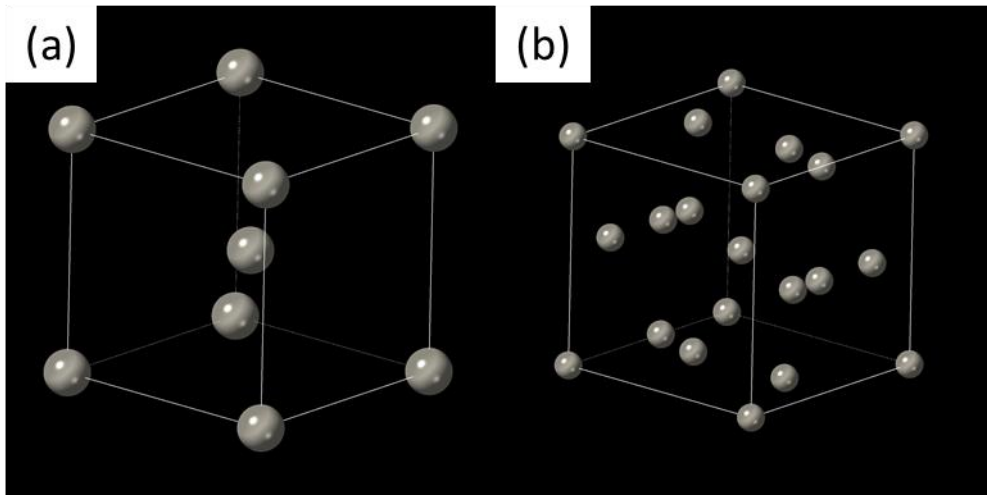

Figure 4.1 Crystal structure of (a) body centered cubic (BCC) α-tungsten and (b) A-15 β-tungsten

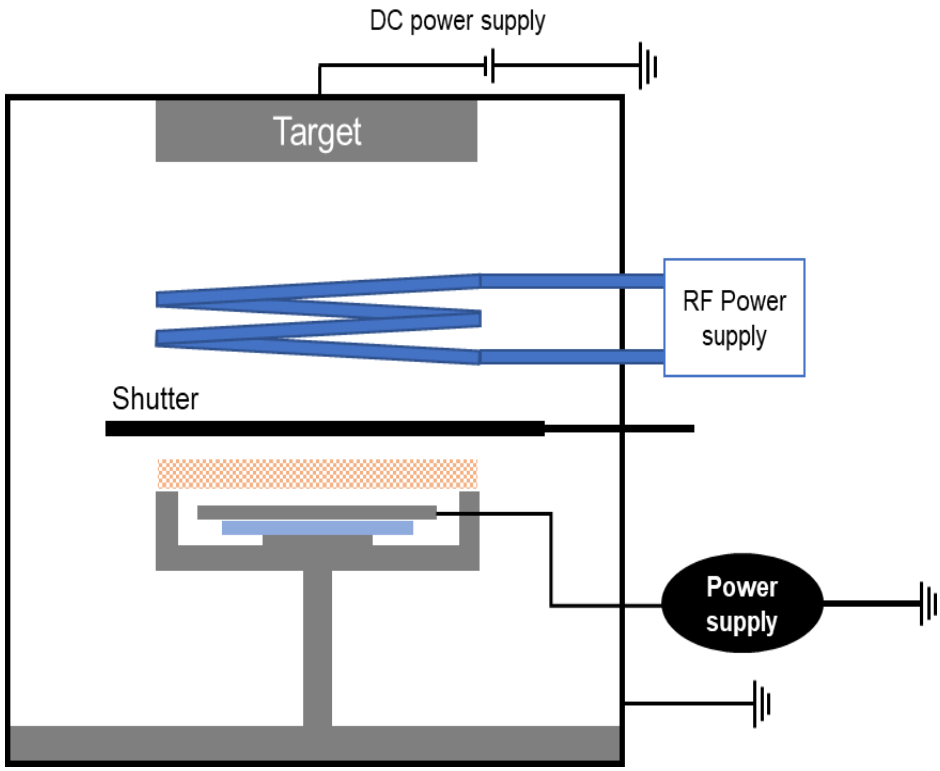

Figure 4.2 Schematics of DC sputtering system assisted by ICP

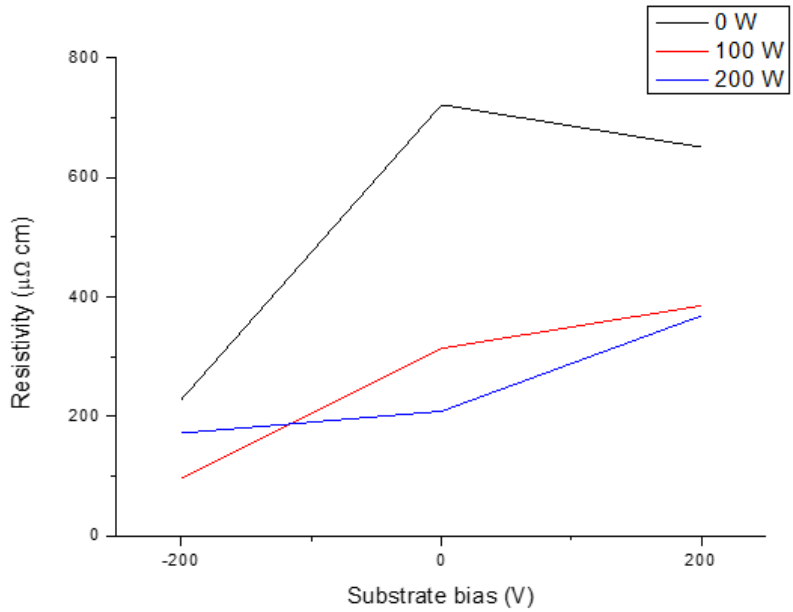

Figure 4.3 Resistivity of the films deposited by DC sputtering assisted by ICP power of 0, 100, and 200 W under the substrate bias of −200, 0, and +200 V

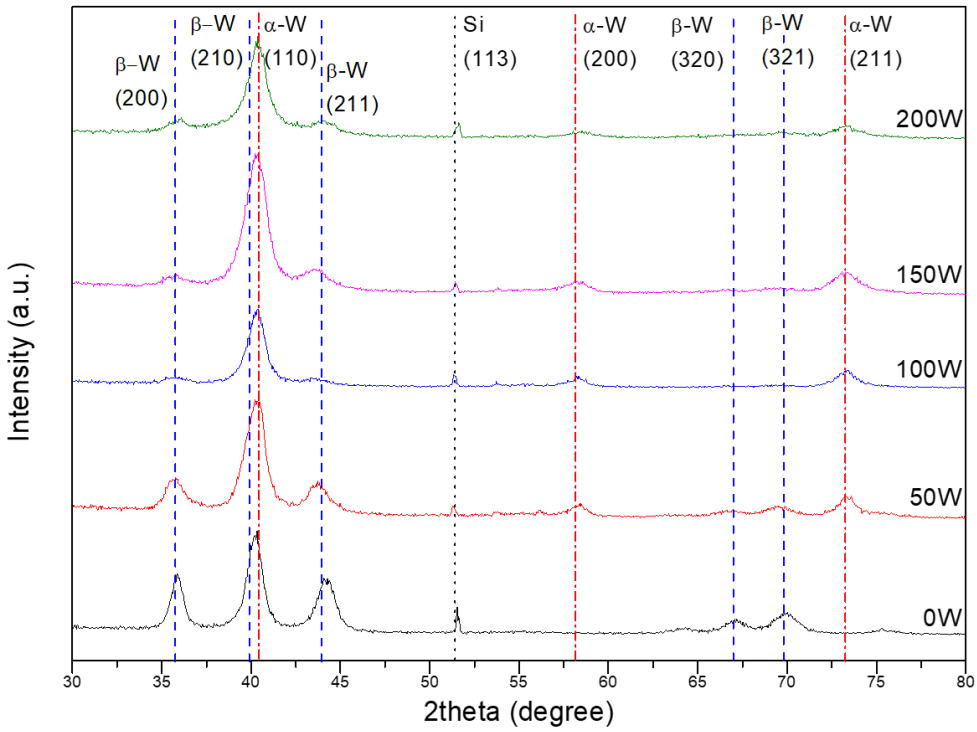

Figure 4.4 GIXRD data of W films deposited under the substrate bias of −200 V and ICP powers of 0, 50, 100, 150, and 200 W

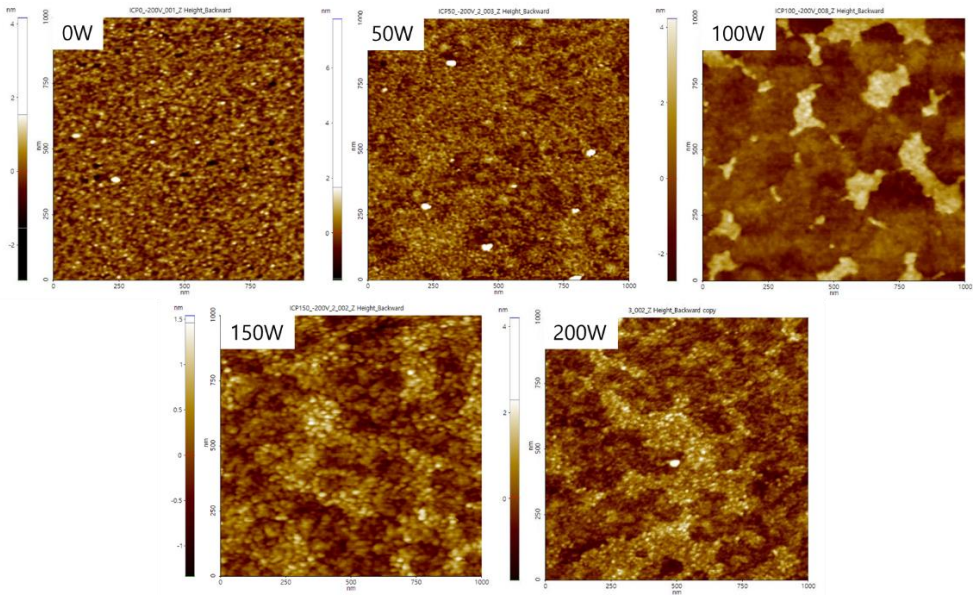

Figure 4.5 Film morphologies of W films deposited under −200 V and various ICP powers obtained by AFM

Bibliography

[1] N. M. Hwang, J. H. Hahn, and D. Y. Yoon, "Charged cluster model in the low pressure synthesis of diamond," *Journal of crystal growth,* vol. 162, no. 1–2, pp. 55–68, 1996.

[2] W.–K. Burton, N. Cabrera, and F. Frank, "The growth of crystals and the equilibrium structure of their surfaces," *Philosophical Transactions of the Royal Society of London. Series A, Mathematical and Physical Sciences,* vol. 243, no. 866, pp. 299–358, 1951.

[3] J. F. Banfield, S. A. Welch, H. Zhang, T. T. Ebert, and R. L. Penn, "Aggregation–based crystal growth and microstructure development in natural iron oxyhydroxide biomineralization products," *Science,* vol. 289, no. 5480, pp. 751–754, 2000.

[4] A. Garscadden, B. Ganguly, P. Haaland, and J. Williams, "Overview of growth and behaviour of clusters and particles in plasmas," *Plasma Sources Science and Technology,* vol. 3, no. 3, p. 239, 1994.

[5] L. Qi, H. Cölfen, and M. Antonietti, "Crystal design of barium sulfate using double-hydrophilic block copolymers," *Angewandte Chemie International Edition,* vol. 39, no. 3, pp. 604–607, 2000.

[6] E. Leite, T. Giraldi, F. Pontes, E. Longo, A. Beltran, and J. Andres, "Crystal growth in colloidal tin oxide nanocrystals induced by coalescence at room temperature," *Appl Phys Lett,* vol. 83, no. 8, pp. 1566–1568, 2003.

[7] Z. Zhang, H. Sun, X. Shao, D. Li, H. Yu, and M. Han, "Three-Dimensionally Oriented Aggregation of a Few Hundred

Nanoparticles into Monocrystalline Architectures," *Advanced Materials,* vol. 17, no. 1, pp. 42-47, 2005.

[8] D. Gebauer, A. Volkel, and H. Colfen, "Stable prenucleation calcium carbonate clusters," *Science,* vol. 322, no. 5909, pp. 1819-1822, 2008.

[9] H. H. Teng, "How ions and molecules organize to form crystals," *Elements,* vol. 9, no. 3, pp. 189-194, 2013.

[10] H.-G. Liao, L. Cui, S. Whitelam, and H. Zheng, "Real-time imaging of Pt3Fe nanorod growth in solution," *science,* vol. 336, no. 6084, pp. 1011-1014, 2012.

[11] J. M. Yuk *et al.*, "High-resolution EM of colloidal nanocrystal growth using graphene liquid cells," *Science,* vol. 336, no. 6077, pp. 61-64, 2012.

[12] N.-M. Hwang and D.-K. Lee, "Charged nanoparticles in thin film and nanostructure growth by chemical vapour deposition," *Journal of Physics D: Applied Physics,* vol. 43, no. 48, p. 483001, 2010.

[13] B. W. Clare, G. Talukder, P. J. Jennings, J. C. L. Cornish, and G. T. Hefter, "Effect of charge on bond strength in hydrogenated amorphous silicon," *Journal of computational chemistry,* vol. 15, no. 6, pp. 644-652, 1994.

[14] H. Fujita, "Atom clusters—new applications of high-voltage electron microscopy “micro-laboratory” to materials science," *Ultramicroscopy,* vol. 39, no. 1-4, pp. 369-381, 1991.

[15] S. Iijima and T. Ichihashi, "Structural instability of ultrafine particles of metals," *Physical review letters,* vol. 56, no. 6, p. 616, 1986.

[16] K.-S. Kim, G. Jang, M. Kim, and N.-M. Hwang, "Origin of

Rapid Coalescence and Active Unstable Fluctuation of Au Nanoparticles under TEM Observation: Electron Bombardment Versus Charge Buildup," *Crystal Growth & Design,* 2022, doi: https://doi.org/10.1021/acs.cgd.2c00644.

[17] S. M. Rossnagel, "Thin film deposition with physical vapor deposition and related technologies," *Journal of Vacuum Science & Technology A,* vol. 21, no. 5, pp. S74–S87, 2003, doi: 10.1116/1.1600450.

[18] N. Selvakumar and H. C. Barshilia, "Review of physical vapor deposited (PVD) spectrally selective coatings for mid- and high-temperature solar thermal applications," *Solar energy materials and solar cells,* vol. 98, pp. 1–23, 2012.

[19] A. Moshfegh, "PVD growth method: physics and technology," *Physics And Technology Of Thin Films: IWTF 2003,* pp. 28–53, 2004.

[20] S. M. Rossnagel, R. Powell, and A. Ulman, *PVD for Microelectronics: Sputter Desposition to Semiconductor Manufacturing*. Elsevier, 1998.

[21] A. Inspektor and P. A. Salvador, "Architecture of PVD coatings for metalcutting applications: A review," *Surface and Coatings Technology,* vol. 257, pp. 138–153, 2014.

[22] J. M. Gregoire, M. B. Lobovsky, M. F. Heinz, F. J. DiSalvo, and R. B. van Dover, "Resputtering phenomena and determination of composition in codeposited films," *Physical Review B,* vol. 76, no. 19, p. 195437, 11/26/ 2007, doi: 10.1103/PhysRevB.76.195437.

[23] D. J. Kester and R. Messier, "Macro-effects of resputtering due to negative ion bombardment of growing thin films," *Journal of Materials Research,* vol. 8, no. 8, pp. 1928–1937,

1993/08/01 1993, doi: 10.1557/JMR.1993.1928.

[24] S. K. Prabha, P. Sreehari, M. Gopal M, and S. P. Sathian, "The effect of system boundaries on the mean free path for confined gases," *AIP Advances,* vol. 3, no. 10, p. 102107, 2013.

[25] J. Lu and C. G. Lee, "Numerical estimates for energy of sputtered target atoms and reflected Ar neutrals in sputter processes," *Vacuum,* vol. 86, no. 8, pp. 1134-1140, 2012.

[26] I. Safi, "Recent aspects concerning DC reactive magnetron sputtering of thin films: a review," *Surface and Coatings Technology,* vol. 127, no. 2-3, pp. 203-218, 2000.

[27] A. Penfold, "Glow discharge sputtering," *by DB Glocker, SI Shah (Institute of Physics Publishing, Bristol, 1995). Sec. A,* vol. 3, 1995.

[28] D. M. Mattox, *Handbook of physical vapor deposition (PVD) processing*. William Andrew, 2010.

[29] C. M. Horwitz, "Radio frequency sputtering—the significance of power input," *Journal of Vacuum Science & Technology A: Vacuum, Surfaces, and Films,* vol. 1, no. 4, pp. 1795-1800, 1983.

[30] R. Tadjine, M. M. Alim, and M. Kechouane, "The erosion groove effects on RF planar magnetron sputtering," *Surface and Coatings Technology,* vol. 309, pp. 573-578, 2017.

[31] J. Sarkar, "Chapter 2-Sputtering and Thin Film Deposition," ed: Boston: William Andrew Publishing, 2014, pp. 93-170.

[32] G. S. Jang, S. M. Ahn, and N.-M. Hwang, "Effects of Sputtering Power, Working Pressure, and Electric Bias on the Deposition Behavior of Ag Films during DC Magnetron Sputtering Considering the Generation of Charged Flux," *Electronic Materials Letters,* vol. 18, no. 1, pp. 57-68, 2022/01/01 2022,

doi: 10.1007/s13391-021-00314-8.

[33] K. Kato, H. Omoto, T. Tomioka, and A. Takamatsu, "Visible and near infrared light absorbance of Ag thin films deposited on ZnO under layers by magnetron sputtering," *Solar energy materials and solar cells,* vol. 95, no. 8, pp. 2352-2356, 2011.

[34] K.-C. Lee, S.-J. Lin, C.-H. Lin, C.-S. Tsai, and Y.-J. Lu, "Size effect of Ag nanoparticles on surface plasmon resonance," *Surface and Coatings Technology,* vol. 202, no. 22-23, pp. 5339-5342, 2008.

[35] Y. Pan, Y. Fan, and J. Niu, "Optical properties of ultra-thin silver films deposited by thermal evaporation and its application in optical filters," *Infrared Physics & Technology,* vol. 104, p. 103123, 2020.

[36] H. K. Park, J. K. Yoon, and K. Kim, "Novel fabrication of Ag thin film on glass for efficient surface-enhanced Raman scattering," *Langmuir,* vol. 22, no. 4, pp. 1626-1629, 2006.

[37] S. H. Park, K. S. Lee, and A. Sivasankar Reddy, "Low emissivity Ag/Ta/glass multilayer thin films deposited by sputtering," *Journal of Applied Physics,* vol. 110, no. 6, p. 063508, 2011.

[38] A. Bittner, H. Seidel, and U. Schmid, "Electromigration resistance and long term stability of textured silver thin films on LTCC," *Microelectronic engineering,* vol. 88, no. 1, pp. 127-130, 2011.

[39] Y. Tsuda, H. Omoto, K. Tanaka, and H. Ohsaki, "The underlayer effects on the electrical resistivity of Ag thin film," *Thin Solid Films,* vol. 502, no. 1-2, pp. 223-227, 2006.

[40] M. Guzman, J. Dille, and S. Godet, "Synthesis and antibacterial activity of silver nanoparticles against gram-positive and

gram−negative bacteria," *Nanomedicine: Nanotechnology, biology and medicine,* vol. 8, no. 1, pp. 37−45, 2012.

[41] J. S. Kim *et al.*, "Antimicrobial effects of silver nanoparticles," *Nanomedicine: Nanotechnology, biology and medicine,* vol. 3, no. 1, pp. 95−101, 2007.

[42] A. R. Shahverdi, A. Fakhimi, H. R. Shahverdi, and S. Minaian, "Synthesis and effect of silver nanoparticles on the antibacterial activity of different antibiotics against Staphylococcus aureus and Escherichia coli," *Nanomedicine: Nanotechnology, Biology and Medicine,* vol. 3, no. 2, pp. 168−171, 2007.

[43] H. Cölfen, *Mesocrystals and nonclassical crystallization*. Wiley England, 2008.

[44] J. J. De Yoreo *et al.*, "Crystallization by particle attachment in synthetic, biogenic, and geologic environments," *Science,* vol. 349, no. 6247, p. aaa6760, 2015, doi: 10.1126/science.aaa6760.

[45] M. Jehannin, A. Rao, and H. Cölfen, "New Horizons of Nonclassical Crystallization," *Journal of the American Chemical Society,* vol. 141, no. 26, pp. 10120−10136, 2019/07/03 2019, doi: 10.1021/jacs.9b01883.

[46] D. Gebauer, A. Völkel, and H. Cölfen, "Stable Prenucleation Calcium Carbonate Clusters," *Science,* vol. 322, no. 5909, p. 1819, 2008, doi: 10.1126/science.1164271.

[47] M. Niederberger and H. Cölfen, "Oriented attachment and mesocrystals: Non−classical crystallization mechanisms based on nanoparticle assembly," *Physical Chemistry Chemical Physics,* 10.1039/B604589H vol. 8, no. 28, pp. 3271−3287, 2006, doi: 10.1039/B604589H.

[48] R. Song, T. Krasia-Christoforou, C. Debus, and H. Cölfen, "Structure and Magnetic Property Control of Copper Hydroxide Acetate by Non-Classical Crystallization," *Small,* vol. 13, no. 9, p. 1602702, 2017/03/01 2017, doi: 10.1002/smll.201602702.

[49] H. A. Abd El-Fattah, I. El-Mahallawi, M. H. Shazly, and W. A. Khalifa, "Microstructure Evolution of NiTi Magnetron Sputtered Thin Film on Different Substrates," *Key Engineering Materials,* vol. 835, pp. 68-74, 2020, doi: 10.4028/www.scientific.net/KEM.835.68.

[50] X. Feng, R. Gao, R. Wang, and G. Zhang, "Non-classical crystal growth on a hydrophobic substrate: learning from bivalve nacre," *CrystEngComm,* 10.1039/D0CE00076K vol. 22, no. 18, pp. 3100-3105, 2020, doi: 10.1039/D0CE00076K.

[51] C. Lizandara-Pueyo, S. Dilger, M. R. Wagner, M. Gerigk, A. Hoffmann, and S. Polarz, "Li-doped ZnO nanorods with single-crystal quality - non-classical crystallization and self-assembly into mesoporous materials," *CrystEngComm,* 10.1039/C3CE41670D vol. 16, no. 8, pp. 1525-1531, 2014, doi: 10.1039/C3CE41670D.

[52] B. Sadri, D. Pernitsky, and M. Sadrzadeh, "Aggregation and deposition of colloidal particles: Effect of surface properties of collector beads," *Colloids and Surfaces A: Physicochemical and Engineering Aspects,* vol. 530, pp. 46-52, 2017/10/05/ 2017, doi: https://doi.org/10.1016/j.colsurfa.2017.07.041.

[53] V. K. Ivanov, P. P. Fedorov, A. Y. Baranchikov, and V. V. Osiko, "Oriented attachment of particles: 100 years of investigations of non-classical crystal growth," *Russian Chemical Reviews,* vol. 83, no. 12, pp. 1204-1222, 2014/12 2014, doi:

10.1070/rcr4453.

[54] D. Grüner and Z. Shen, "Ordered coalescence of nano-crystals during rapid solidification of ceramic melts," *CrystEngComm,* 10.1039/C1CE05436H vol. 13, no. 17, pp. 5303-5305, 2011, doi: 10.1039/C1CE05436H.

[55] M. Hu, J.-S. Jiang, R.-P. Ji, and Y. Zeng, "Prussian Blue mesocrystals prepared by a facile hydrothermal method," *CrystEngComm,* 10.1039/B911613N vol. 11, no. 11, pp. 2257-2259, 2009, doi: 10.1039/B911613N.

[56] B. Jin, Z. Liu, and R. Tang, "Recent experimental explorations of non-classical nucleation," *CrystEngComm,* 10.1039/D0CE00480D vol. 22, no. 24, pp. 4057-4073, 2020, doi: 10.1039/D0CE00480D.

[57] D. J. Banner *et al.*, "In Situ Liquid-Cell TEM Observation of Multiphase Classical and Nonclassical Nucleation of Calcium Oxalate," *Advanced Functional Materials,* https://doi.org/10.1002/adfm.202007736 vol. 31, no. 18, p. 2007736, 2021/05/01 2021, doi: https://doi.org/10.1002/adfm.202007736.

[58] J. Cookman, V. Hamilton, S. R. Hall, and U. Bangert, "Non-classical crystallisation pathway directly observed for a pharmaceutical crystal via liquid phase electron microscopy," *Scientific Reports,* vol. 10, no. 1, p. 19156, 2020/11/05 2020, doi: 10.1038/s41598-020-75937-2.

[59] N. M. Hwang, *Non-classical crystallization of thin films and nanostructures in CVD and PVD processes*. Dordrecht: Springer, 2016.

[60] W. K. Youn, S. S. Lee, J. Y. Lee, C. S. Kim, N. M. Hwang, and S. Iijima, "Comparison of the Deposition Behavior of Charged

Silicon Nanoparticles between Floating and Grounded Substrates," (in English), *J. Phys. Chem. C,* Article vol. 118, no. 22, pp. 11946-11953, Jun 2014, doi: 10.1021/jp5001144.

[61] S.-W. Park, J.-S. Jung, K.-S. Kim, K.-H. Kim, and N.-M. Hwang, "Effect of Bias Applied to the Substrate on the Low Temperature Growth of Silicon Epitaxial Films during RF-PECVD," *Crystal Growth & Design,* vol. 18, no. 10, pp. 5816-5823, 2018/10/03 2018, doi: 10.1021/acs.cgd.8b00384.

[62] Y. Lee, H. N. Han, W. Kim, and N. M. Hwang, "Effect of Bipolar Charging of SiH4 on the Growth Rate and Crystallinity of Silicon Films Grown in the Atmospheric Pressure Chemical Vapor Deposition Process," (in English), *Electronic Materials Letters,* vol. 16, no. 4, pp. 385-395, Jul 2020, doi: 10.1007/s13391-020-00217-0.

[63] D. Kim, D. Kim, J. H. Kwon, K. S. Kim, and N. M. Hwang, "Generation of Charged SiC Nanoparticles During HWCVD Process," (in English), *Electronic Materials Letters,* vol. 16, no. 5, pp. 498-505, Sep 2020, doi: 10.1007/s13391-020-00230-3.

[64] I.-D. Jeon, D.-Y. Kim, and N.-M. Hwang, "Spontaneous generation of charged atoms or clusters during thermal evaporation of silver," *Zeitschrift für Metallkunde,* vol. 96, no. 2, pp. 186-190, 2005/02/01 2005, doi: 10.3139/146.101018.

[65] G.-S. Jang, D.-Y. Kim, and N.-M. Hwang, "The Effect of Charged Ag Nanoparticles on Thin Film Growth during DC Magnetron Sputtering," *Coatings,* vol. 10, no. 8, 2020, doi: 10.3390/coatings10080736.

[66] J.-H. Kwon, D.-Y. Kim, and N.-M. Hwang, "Generation of Charged Ti Nanoparticles and Their Deposition Behavior with

a Substrate Bias during RF Magnetron Sputtering," *Coatings,* vol. 10, no. 5, 2020, doi: 10.3390/coatings10050443.

[67] J. H. Kwon, D. Kim, K. S. Kim, and N. M. Hwang, "Preparation of Highly (002) Oriented Ti Films on a Floating Si (100) Substrate by RF Magnetron Sputtering," (in English), *Electronic Materials Letters,* vol. 16, no. 1, pp. 14-21, Jan 2020, doi: 10.1007/s13391-019-00182-3.

[68] C. Zhang, W. Ding, H. Wang, W. Chai, and D. Ju, "Influences of working pressure on properties for TiO2 films deposited by DC pulse magnetron sputtering," *Journal of Environmental Sciences,* vol. 21, no. 6, pp. 741-744, 2009/01/01/ 2009, doi: https://doi.org/10.1016/S1001-0742(08)62334-7.

[69] M. Seidl, J. P. Perdew, M. Brajczewska, and C. Fiolhais, "Ionization energy and electron affinity of a metal cluster in the stabilized jellium model: Size effect and charging limit," *The Journal of chemical physics,* vol. 108, no. 19, pp. 8182-8189, 1998.

[70] F. T. Muniz, M. A. Miranda, C. Morilla Dos Santos, and J. M. Sasaki, "The Scherrer equation and the dynamical theory of X-ray diffraction," *Acta Crystallographica. section A, Foundations and Advances,* vol. 72, no. Pt 3, pp. 385-90, May 1 2016, doi: 10.1107/S205327331600365X.

[71] G. S. Jang, D. Y. Kim, and N. M. Hwang, "Dependence of the Generation Behavior of Charged Nanoparticles and Ag Film Growth on Sputtering Power during DC Magnetron Sputtering," (in English), *Electronic Materials Letters,* vol. 17, no. 2, pp. 172-180, Mar 2021, doi: 10.1007/s13391-020-00263-8.

[72] S. M. Ahn, G. S. Jang, D. Y. Kim, and N.-M. Hwang, "Effects of Substrate Bias and Ar Pressure on Growth of α-phase in

W Thin Films Deposited by RF Magnetron Sputtering," *Electronic Materials Letters,* 2022/12/29 2022, doi: 10.1007/s13391-022-00399-9.

[73] C. K. Hu, R. Rosenberg, and K. Y. Lee, "Electromigration path in Cu thin-film lines," (in English), *Appl Phys Lett,* vol. 74, no. 20, pp. 2945-2947, May 17 1999, doi: https://doi.org/10.1063/1.123974.

[74] J. R. Lloyd, J. Clemens, and R. Snede, "Copper metallization reliability," (in English), *Microelectron Reliab,* vol. 39, no. 11, pp. 1595-1602, Nov 1999, doi: https://doi.org/10.1016/S0026-2714(99)00177-8.

[75] K. Ganesh and V. H. Gaidhane, "Tungsten as an Interconnect Material for Next-Generation IC Design," (in English), *2020 Ieee International Iot, Electronics and Mechatronics Conference (Iemtronics 2020),* pp. 443-448, 2020, doi: 10.1109/IEMTRONICS51293.2020.9216452.

[76] D. Choi *et al.*, "Phase, grain structure, stress, and resistivity of sputter-deposited tungsten films," *Journal of Vacuum Science & Technology A: Vacuum, Surfaces, and Films,* vol. 29, no. 5, p. 051512, 2011, doi: https://doi.org/10.1116/1.3622619.

[77] A. K. Sinha, "Topologically close-packed structures of transition metal alloys," *Progress in Materials Science,* vol. 15, no. 2, pp. 81-185, 1972/01/01/ 1972, doi: https://doi.org/10.1016/0079-6425(72)90002-3.

[78] D. Choi, "Phase transformation in thin tungsten films during sputter deposition," *Microelectronic Engineering,* vol. 183, pp. 19-22, 2017.

[79] P. Petroff, T. T. Sheng, A. K. Sinha, G. A. Rozgonyi, and F. B.

Alexander, "Microstructure, Growth, Resistivity, and Stresses in Thin Tungsten Films Deposited by Rf Sputtering," (in English), *Journal of Applied Physics,* vol. 44, no. 6, pp. 2545–2554, 1973, doi: https://doi.org/10.1063/1.1662611.

[80] Q. Hao, W. Chen, and G. Xiao, "Beta (β) tungsten thin films: Structure, electron transport, and giant spin Hall effect," *Appl Phys Lett,* vol. 106, no. 18, p. 182403, 2015, doi: https://doi.org/10.1063/1.4919867.

[81] P. Petroff and W. Reed, "Resistivity behavior and phase transformations in β–W thin films," *Thin Solid Films,* vol. 21, no. 1, pp. 73–81, 1974, doi: https://doi.org/10.1016/0040-6090(74)90092-3.

[82] F. T. N. Vullers and R. Spolenak, "Alpha- vs. beta-W nanocrystalline thin films: A comprehensive study of sputter parameters and resulting materials' properties," (in English), *Thin Solid Films,* vol. 577, pp. 26–34, Feb 27 2015, doi: https://doi.org/10.1016/j.tsf.2015.01.030.

[83] P. Collot *et al.*, "Physicochemical properties in tungsten films deposited by radio-frequency magnetron sputtering," *Journal of Vacuum Science & Technology A: Vacuum, Surfaces, and Films,* vol. 6, no. 4, pp. 2319–2325, 1988.

[84] M. Hugon, F. Varniere, B. Agius, M. Froment, C. Arena, and J. Bessot, "Stresses, microstructure and resistivity of thin tungsten films deposited by RF magnetron sputtering," *Applied surface science,* vol. 38, no. 1–4, pp. 269–285, 1989, doi: https://doi.org/10.1016/0169-4332(89)90548-5.

[85] Y. Shen, Y. Mai, Q. Zhang, D. McKenzie, W. McFall, and W. McBride, "Residual stress, microstructure, and structure of tungsten thin films deposited by magnetron sputtering,"

Journal of Applied Physics, vol. 87, no. 1, pp. 177–187, 2000.

[86] B. Chapman and J. Vossen, "Glow discharge processes: sputtering and plasma etching," *Physics Today,* vol. 34, no. 7, p. 62, 1981.

[87] U. Pietsch, V. Holy, and T. Baumbach, *High-resolution X-ray scattering: from thin films to lateral nanostructures*. New York: Springer Science & Business Media, 2004.

[88] H. Marom and M. Eizenberg, "The effect of surface roughness on the resistivity increase in nanometric dimensions," *Journal of applied physics,* vol. 99, no. 12, p. 123705, 2006, doi: https://doi.org/10.1063/1.2204349.

[89] D.-Y. Kim, J.-H. Kwon, G.-S. Jang, and N.-M. Hwang, "Effect of Pressure on the Film Deposition during RF Magnetron Sputtering Considering Charged Nanoparticles," *Coatings,* vol. 11, no. 2, p. 132, 2021, doi: https://doi.org/10.3390/coatings11020132.

[90] J. Dalla Torre *et al.*, "Microstructure of thin tantalum films sputtered onto inclined substrates: Experiments and atomistic simulations," *Journal of applied physics,* vol. 94, no. 1, pp. 263–271, 2003, doi: https://doi.org/10.1063/1.1579112.

[91] S.-w. Park, G.-s. Jang, K.-s. Kim, and N.-m. Hwang, "Comparison of plasma effect on dewetting kinetics of Sn films between grounded and floating substrates," *Electronic Materials Letters,* vol. 16, no. 1, pp. 72–80, 2020, doi: https://doi.org/10.1007/s13391-019-00190-3.

[92] S. Lee, J. H. Park, C. G. Park, D.-Y. Jeong, and N.-M. Hwang, "Generation of positively charged nanoparticles by fracto-emission and their deposition into films during aerosol deposition," *Applied Surface Science,* vol. 593, p. 153466,

2022, doi: https://doi.org/10.1016/j.apsusc.2022.153466.

[93] T. Yamamoto, M. Hara, and Y. Hatano, "Effects of fabrication conditions on the microstructure, pore characteristics and gas retention of pure tungsten prepared by laser powder bed fusion," *International Journal of Refractory Metals and Hard Materials,* vol. 95, p. 105410, 2021.

[94] D. Choi and K. Barmak, "On the potential of tungsten as next-generation semiconductor interconnects," *Electronic Materials Letters,* vol. 13, pp. 449-456, 2017.

[95] C. Christou and Z. Barber, "Ionization of sputtered material in a planar magnetron discharge," *Journal of Vacuum Science & Technology A: Vacuum, Surfaces, and Films,* vol. 18, no. 6, pp. 2897-2907, 2000.

[96] Y. Setsuhara, M. Kamai, and S. M. Musil, "Inductively-coupled-plasma-assisted planar magnetron discharge for enhanced ionization of sputtered atoms," *Japanese journal of applied physics,* vol. 36, no. 7S, p. 4568, 1997.

[97] B. B. Sahu, S. B. Jin, P. J. Xiang, J. B. Kim, and J. G. Han, "Effect of inductively coupled plasma and plasma parameters on magnetron sputtered Al-Doped ZnO highly conductive thin films at low-temperature," *Journal of Applied Physics,* vol. 123, no. 20, p. 205107, 2018.

국문 초록

최근 DC 및 RF 마그네트론 스퍼터링 공정에서 하전된 플럭스의 생성과 필름 증착에 대한 하전된 플럭스의 영향이 연구되었다. 따라서 하전된 플럭스 생성에 영향을 미치는 증착 파라미터를 DC 및 RF 스퍼터링 시스템에서 연구하였다. 특히, 플라즈마를 생성하기 위해 사용되는 아르곤(Ar) 압력과 기판 바이어스 하에서의 하전 거동을 연구하였다.

먼저, DC 마그네트론 스퍼터링에 의해 증착된 은(Ag) 박막의 성장 속도, 결정도 및 비저항에 대한 스퍼터링 파워, 작동 압력 및 바이어스의 영향을 연구하였다. 박막은 20, 50, 100, 200 W의 스퍼터링 파워, 2.5, 5, 10, 20 mTorr의 공정 압력과 −300, 0, +300 V의 기판 바이어스 공정 조건 하에서 30분 동안 증착되었다. 모든 스퍼터링 파워에서 박막의 성장률은 양의 바이어스에 의해 증가한 반면, 음의 바이어스에 의해 감소하였다. 예를 들어, 스퍼터링 파워 100W와 공정 압력 2.5mTorr에서, 박막의 두께는 각각 −300, 0, +300V에서 346, 378, 416nm였다. 기판 바이어스 효과는 공정 압력이 감소함에 따라 두드러졌다. 바이어스에 따른 박막성장속도의 변화를 고려하면 음으로 하전된 플럭스의 양은 대략 10%로 추정된다. 공정 압력이 감소함에 따라 증착된 막의 결정화도는 양의 바이어스에 의해 증가한 반면, 네거티브 바이어스에 의해 감소하였다. 박막의 저항값도 같은 경향을 보였다. 은 필름의 증착 거동의 이러한 변화는 하전된 플럭스의 효과로 이해할 수 있다.

또한, RF 마그네트론 스퍼터링에 의해 증착된 텅스텐(W) 막에 아르곤

가스 압력과 기판 바이어스가 미치는 영향을 조사하였다. 텅스텐은 일반적으로 반도체용 구리 배선을 대체하는 재료로 사용되고 있다. 실온에서 스퍼터링에 의해 증착된 텅스텐 박막은 상대적으로 저항이 높은 준안정 β상을 갖고, 특정 조건 하에서 상대적으로 저항이 낮은 안정한 α상으로 변환되는 것이 일반적으로 관찰되어 왔다. 20 mTorr 및 −100 V의 기판 바이어스 하에서 1초간의 짧은 증착 초기 단계에서, 투과 전자 현미경(TEM)을 사용하여 β상 텅스텐의 나노 크기의 입자를 관찰하였다. 그러나 동일한 압력 및 바이어스 조건에서 증착 시간이 10분으로 증가함에 따라 텅스텐 필름은 α상과 β상이 공존하였다. α상 텅스텐의 비율은 음의 바이어스가 −100에서 −200V로 증가함에 따라 더 증가하였다. 또한 바이어스가 +100에서 −100V로 변경됨에 따라 필름 밀도가 증가하고 표면 거칠기가 감소했다. 이러한 결과는 음의 바이어스가 β상에서 α상으로 텅스텐의 상을 변화시킨 것을 나타낸다. α상 텅스텐의 형성과 필름의 저항값에 대한 바이어스 효과는 압력이 증가함에 따라 더욱 두드러졌다.

또한, DC 스퍼터링 시 이온화율을 높이기 위해서 DC 마그네트론 스퍼터링 시스템에 유도 결합 플라즈마(ICP)를 설치하였다. 텅스텐 박막은 −200, 0, +200V의 기판 바이어스 조건에서 ICP 파워를 0에서 200W로 증가시키면서 증착되었다. ICP 파워가 증가하고 기판에 음의 바이어스가 가해질 때 α상 텅스텐의 성장이 향상되고 텅스텐 막의 저항이 감소하였다. 그러나 XRD(X−ray diffraction) 데이터와 비저항 측정 결과로부터 α상 텅스텐의 성장을 위한 최적화된 공정 조건이 있음을 알 수

있었다. 이 연구에서 가장 낮은 저항을 가지는 텅스텐 박막은 ICP 파워가 100W이고 기판 바이어스가 −200V일 때 얻어졌다.